University of Wollongong

Research Online

University of Wollongong Thesis Collection 2017+

University of Wollongong Thesis Collections

2018

Cerium oxide nanoparticles: A study of Ce3+ ion influence on radioprotection

Lee Taylor
University of Wollongong

Follow this and additional works at: https://ro.uow.edu.au/theses1

University of Wollongong

Copyright Warning

You may print or download ONE copy of this document for the purpose of your own research or study. The University does not authorise you to copy, communicate or otherwise make available electronically to any other person any copyright material contained on this site.

You are reminded of the following: This work is copyright. Apart from any use permitted under the Copyright Act 1968, no part of this work may be reproduced by any process, nor may any other exclusive right be exercised, without the permission of the author. Copyright owners are entitled to take legal action against persons who infringe their copyright. A reproduction of material that is protected by copyright may be a copyright infringement. A court may impose penalties and award damages in relation to offences and infringements relating to copyright material. Higher penalties may apply, and higher damages may be awarded, for offences and infringements involving the conversion of material into digital or electronic form.

Unless otherwise indicated, the views expressed in this thesis are those of the author and do not necessarily represent the views of the University of Wollongong.

Recommended Citation

Taylor, Lee, Cerium oxide nanoparticles: A study of Ce3+ ion influence on radioprotection, Masters of Science (Research) thesis, Centre for Medical Radiation Physics, University of Wollongong, 2018. https://ro.uow.edu.au/theses1/445

Research Online is the open access institutional repository for the University of Wollongong. For further information contact the UOW Library: research-pubs@uow.edu.au

University of Wollongong

MASTER THESIS

Cerium oxide nanoparticles: A study of Ce^{3+} ion influence on radioprotection.

Author:

Lee Taylor

Supervisors:

Prof. Michael Lerch

Dr Moeava Tehei

A. P. Konstantin Konstantinov

A thesis submitted in fulfilment of the requirements

for the degree of Master of Science - Research

in the

Centre for Medical Radiation Physics

School of Physics

November 2018

Statement of Originality

This is to certify that the work described in this thesis is entirely my own, except where due reference is made in text.

No work in this thesis has been submitted for a degree to any other university or institution.

Signed,

Lee M. Taylor

29th of March 2018

Abstract

In 2011 Celardo et al. [1] demonstrated that the antioxidant capacity of cerium oxide nanoparticles (CeOx NPs) was dependent on the population of Ce^{3+} ions within the nanoparticle. In the cellular environment the nanoparticles were able to quench free radicals through cyclic redox reactions of the Ce^{3+} ions. The consequence being the larger the Ce^{3+} ion population of included NPs the larger the resultant cell growth of the assayed cell line. The goal of this thesis was to reproduce these findings and determine whether this dependency also translated to radiation protection efficacy under megavoltage (MV) x-ray radiation. Two-thirds of cell death inflicted by MV x-rays is achieved through the generation of free radical species. It therefore stands that controlling the population of Ce^{3+} ions within CeOx NPs should control their ability to protect against radiation damage.

Cerium oxide nanocrystalline particles were synthesised by spray pyrolysis. To modulate the population of Ce^{3+} ions the NPs were doped with iron (Fe^{3+}). 5%, 10% and 20% atomic concentrations variants were synthesised. The nanoparticles were characterised using x-ray diffraction (XRD), optical emission spectroscopy (OES), transmission electron microscope (TEM) and x-ray photoelectron spectroscopy (XPS). XRD showed all crystallites to be of a single phase and built of a cubic fluorite structure consistent with the formation of cerium oxide. Crystallites were all within the range of 5-10 nm. A reducing lattice parameter with increased iron doping confirmed the inclusion of the Fe^{3+} ions within the cerium oxide lattice. Rietveld refinement determine the minimum lattice parameter to be 5.416 Å suggesting inclusion of Ce^{3+} ions for all particles. Actual Fe^{3+} doping was found to be within 0.5% of target concentration for all particles except the 20% iron doped variant which experienced 1% iron loss as a result of surpassing the crystal solubility limit.

Global assessment of nanocrystalline particles using XPS showed a decreasing population of Ce^{3+} ions with increasing Fe^{3+} ion inclusion. 18% atomic concentration of Ce^{3+} ions in pure cerium oxide particles reduced to ~8% for the 20 % iron doped variant.

Clonogenic assays using 9L gliosarcoma cells assessed the ability of CeOx NPs to boost cell growth and protect against megavoltage x-ray damage. With no radiation pure CeOx NPs provided a 10% boost to cell growth. When 8 Gy of 10 MV x-rays was delivered to the cell monolayer the CeOx NP inclusion improved cell survival by 75%. Increasing the radiation survival fraction from 0.12 to 0.22. The inclusion of the 5% Fe doped CeOx NPs boosted cell growth by 6% and increased the radiation survival fraction by 20%. 10% Fe doped CeOx NPs did not significantly boost cell growth or improve radiation survival fraction. 20% Fe doped CeOx NPs reduced cell growth by 12% and were not used in radiation studies.

Overall these studies suggest that radioprotection efficacy of cerium oxide nanoparticles is dependent on the population of Ce^{3+} ions. The correlation between nanoparticle Ce^{3+} population, cell growth and cell survival fraction provide clear and comprehensive evidence of this dependency.

Acknowledgements

This research has been conducted with the support of the Australian Government Research Training Program Scholarship.

Thanks to all who helped, especially Stephanie, Dean, Kathrin, Marjorie and Mike.

Finally, special thanks to my wonderful parents, Pene and Ian, for all their support and belief through the painful process that is a Scientific Thesis.

List of Contents

List of Figures and Tables

Abbreviations

CeOx NP	**Ce**rium **Ox**ide **N**ano **P**article
XRD	**X**-ray **D**iffraction
TGA	**T**hermal **G**ravimetric **A**nalysis
EDX	**E**nergy **D**ispersive **X**-ray spectroscopy
OES	**O**ptical **E**mission **S**pectroscopy
TEM	**T**ransmission **E**lectron **M**icroscopy
XPS	**X**-ray **P**hotoelectron **S**pectroscopy
GBM	**G**lio **B**lastoma **M**ultiforme
DPBS	**D**ulbecco's **P**hosphate **B**uffered **S**olution
DMEM	**D**ulbecco's **M**odified **E**agle **M**edia
HBSS	**H**ank's **B**alanced **S**alt **S**olution
FBS	**F**oetal **B**ovine **S**erum
DNA	**D**eoxyribo **N**ucleic **A**cid
BSC	**B**iological **S**afety **C**abinet
ROS	**R**eactive **O**xygen **S**pecies
SOD	**S**uper **O**xide **D**ismutase
EDTA	**E**thylene **D**iamine **T**etra **A**cetic acid
PE	**P**lating **E**fficiency
SF	**S**urvival **F**raction
PER	**P**erformance **E**nhancement **R**atio
CT	**C**omputed **T**omography
TPS	**T**reatment **P**lanning **S**oftware
EBRT	**E**xternal **B**eam **R**adiation **T**herapy
VMAT	**V**olumetric **M**odulated **A**rc **T**herapy

SABR	**S**tereotactic **A**blative **B**ody **R**adiotherapy
TR	**T**herapeutic **R**atio

Chapter 1

Hypothesis and Objectives

1.1 Hypothesis of thesis

The radioprotection efficacy of cerium oxide nanoparticles is dependent upon the population of Ce^{3+} ion within the crystal lattice.

1.2 Objectives of thesis

The fundamental objectives and aims of this thesis were to:

- synthesise pure and iron doped cerium oxide nanoparticles,
- characterise pure and iron doped cerium oxide nanoparticles;
- assess the antioxidant behaviour of pure and iron doped cerium oxide nanoparticles included in a 9L cell line; and
- assess the radioprotection given to a 9L cell line by pure and iron doped cerium oxide nanoparticles when irradiated with 10 MV x-rays.

Chapter 2

Literature Review

2.1 Cancer

Cancer is a disorder characterised by the continual proliferation of cells. Ordinarily cell death would counter cell growth however, cancer cells divide quicker than they die; invading adjacent tissues and damaging the organs of an organism. This outcome arises from the mutation of the genetic material within cancer cells and an inability of the body to recognise and destroy the cancer cells [2]. Cancer cells can be characterised by the following unique features:

- *Clonal origin.* Most cancer cells arise from one abnormal cell formed due to field damage or heritable defects in some genes.
- *Immortality.* Unlike normal cells cancer cells can undergo an unlimited number of divisions. One of the mechanisms for immortality is associated with telomeres; the tips of chromosomes. In normal differentiated cells telomeres shorten with division until the cell goes into a resting state and consequently dies. In cancer cells and stem cells the telomerase enzyme renews telomeres allowing the cells to proliferate indefinitely.
- *Genetic instability*. This situation is caused by defects in the DNA repair process and in the DNA mismatch recognition, which results in the heterogeneity of cancer cells. Cancer cells form clones that gradually respond less to proliferation control and become hardier in foreign environments.
- *Loss of contact inhibition*. In-vitro studies show normal cells stop dividing once they have exhausted space no matter the quantity of growth factors and nutritional elements. Cancer

cells continue to divide independent of surface contact and will grow in multiple layers until resources are exhausted causing their subsequent death.

- *Metastasis.* This feature is not found in benign tumours and normal cells. Metastasis is caused by breakdown in adherence mechanism to the extracellular matrix, intercellular interactions and destruction of connective membranes such as the basal layer.

The 2017 report by the Australian Institute of Health and Welfare (AIHW) estimated that 134,174 Australians will be diagnosed with cancer for the year. More than half of those cases would be for males and 71% for those aged 60 years and over. The most commonly reported cancers in this year would be, in order of prevalence, breast, bowel, prostate and melanoma cancer. The report finishes by noting, that according to the World Health Organization (WHO) people living in Australia generally had better cancer survival than people in other regions about the world. This is attributed to government funding into health education, early detection programs and access to comprehensive healthcare [3].

2.2 Cellular effects of radiation

All molecules within a cell can be damaged by ionising radiation (IR) however, DNA molecules that carry genetic information relating to cell division and growth are the most critical structures. Over the years target studies on individual cells have shown radiation to be most lethal when it targets the nucleus of a cell [4]. While there are many copies of mRNA, water and proteins there are only two copies of DNA. Radiation may damage one or several locations on the helix structure resulting in damage to bases and/or the phosphate backbone strands. Depending on the extent of the damage several outcomes are possible:

1. The DNA is successfully repaired and the cell continues to proliferate
2. The DNA is not repaired and the cell dies (controlled or uncontrolled)
3. The DNA is incorrectly repaired leading to death in a future generation (controlled or uncontrolled)
4. The DNA is incorrectly repaired leading to the formation of cancer

The interaction of therapeutic x-ray beams (MV) in tissue is primarily down to Compton scatter with minor contribution from photoelectric absorption and pair production. Photons ionise/excite electrons within molecules and macromolecules contained within the cell. The ejection of these electrons affects chemical change, causing bonds to be broken. If enough bonds are broken within the DNA or repair molecules the cell may be unable to function correctly leading to apoptotic or mitotic death [5].

The cell damage occurs through direct and indirect interaction as shown in Figure 2-1. Direct action sees 'ejected' secondary electrons cause further ionisation in the molecules they collide with, progressively slowing down as they go. At the end of these electron tracks there is clustering of ionisation events [6]. The clustering causes many breaks along the DNA helix structure. It has been found that breaks to both strands within 4 base pairs will greatly increase chance of cell death [7].

Indirect damage is the result of interaction of IR with the cytoplasm which create reactive chemical species that attack the DNA and other vital structures as shown in Figure 2-1. As much of a cell is made of water the majority of indirect damage is mediated through the ionisation of the water molecule. The water molecule is ionised to produce an ion pair of H_2O^+ and H_2O^-. Each is unstable and dissociates to form another ion and a free radical as shown in chemical equation 2-1 and Equation 2-2. Free radicals are neutral molecules with a lone electron and highly reactive.

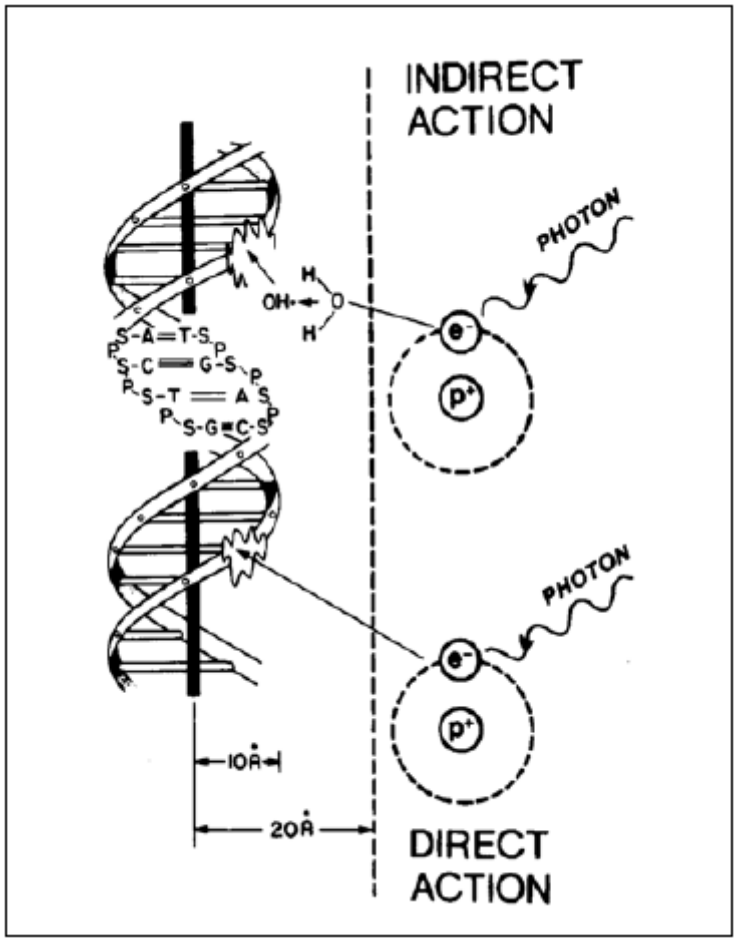

Figure 2-1: DNA is damaged direct by secondary electrons and indirectly by free radicals [8].

Free radicals can work as oxidising or reducing agents by combining directly with macromolecules like DNA. H^+ and OH^- ions do not typically produce much biological damage owing to the short lifetime of ~10^{-10}s and their tendency to recombine to form water (Equation 2-3).

Equation 2-1 $$H_2O^+ \rightarrow H^+ + OH\bullet$$

Equation 2-2 $$H_2O^- \rightarrow H\bullet + OH^+$$

Equation 2-3 $$H^+ + OH^- \rightarrow H_2O$$

The free radicals H• and OH• may also recombine to form water (Equation 2-4) however in the presence of oxygen this is less likely to occur as oxygen stabilises free radicals. Instead these radicals could form hydrogen peroxide (Equation 2-5), a natural occurring chemical product of metabolism that is linked to apoptotic death. Oxygen itself could react with a hydrogen radical to form a hydroperoxyl radical (Equation 2-6) or it could be reduced by a lone electron to form the superoxide ion (Equation 2-7). There are a multitude of further ions and radicals that can be produced; these include nitrous and organic compounds. While the lifetime of these species might only be ~10^{-5} s they can diffuse throughout the cell causing damage at locations remote form their origin [9].

Equation 2-4 $$H\bullet + OH\bullet \rightarrow H_2O$$

Equation 2-5 $$OH\bullet + OH\bullet \rightarrow H_2O_2$$

Equation 2-6 $$H\bullet + O_2 \rightarrow HO_2$$

Equation 2-7 $$O_2 + e^- \rightarrow O_2\bullet^-$$

Roughly two thirds of cell damage caused by MV photons on mammalian cells lines is caused by in-direct ionisation [10]. The dependence of MV photons on indirect action makes it less effective when dealing with hypoxic cells however in most cases this dependency can be greatly reduced through fractionation.

2.3 Radiation Therapy

Radiation therapy or radiotherapy uses ionising radiation to deliver a prescribed dose to a tumour while ensuring radiation dose to surrounding normal tissue is kept as low as possible [11]. The most commonly used radiation therapy at present in Australia is external beam radiation therapy (EBRT) using megavoltage (MV) x-ray beams.

Less utilised are treatments using kilovoltage x-rays, electrons and radioactive sources. Proton therapy will be available in Australia in the near future [12]. It has been reported that currently in Australia the therapy utilisation rate for radiation therapy is approximately 48% [13].

Radiotherapy may be the primary treatment modality or may be used in conjunction with another therapy to:

- destroy primary and metastatic solid tumours,
- shrink a tumour prior to surgical excision,
- destroy subclinical disease about a margin after a surgical excision,
- treat subclinical disease along a known disease pathway.
- salvage a treatment after a cancer recurrence.
- boost tumour response when delivered concurrently with chemotherapy or another agent.
- alleviate pain for a palliative patient by affecting rapid tumour response.

Radiation therapy has a major impact on local cancer control and is highly effective treatment for control of cancer symptoms such as pain and bleeding [14].

2.4 Radiotherapy technology and technique

To reduce normal tissue damage radiotherapy treatment delivers absorbed dose to the target tissue in parts known as fractions. A common fractionation regimen sees 2 Gy of absorbed dose delivered daily over the course of several weeks. The benefits of fractionation are:

- *Repair*. By ensuring a minimum of 6 - 8hrs between fractions normal tissue is given adequate time to repair sub lethal damage (SLD).

- *Redistribution.* Fractionation ensures that cancer cells will be in a radiosensitive phase of the cell cycle for multiple fractions.
- *Reoxygenation.* Oxygenation is important to assure high radiosensitivity. Rapid growing tumours can have inadequate vasculature causing hypoxic peripheral cells. Cell death inflicted by radiation increases supply of blood flow to these dormant (quiescent) cells [15].

The quality of fractionated treatment is quantified using the Therapeutic Ratio (TR). The TR is the ratio of tumour control to normal tissue complication for a treatment dose. Using past patient data, the probability of tumour control and normal tissue damage (toxicity) can be graphed for each site, treatment regimen and early/late tissue toxicity. Over a period of 5 -10 years fractionation regimens can be compared to determine optimal radiation therapies.

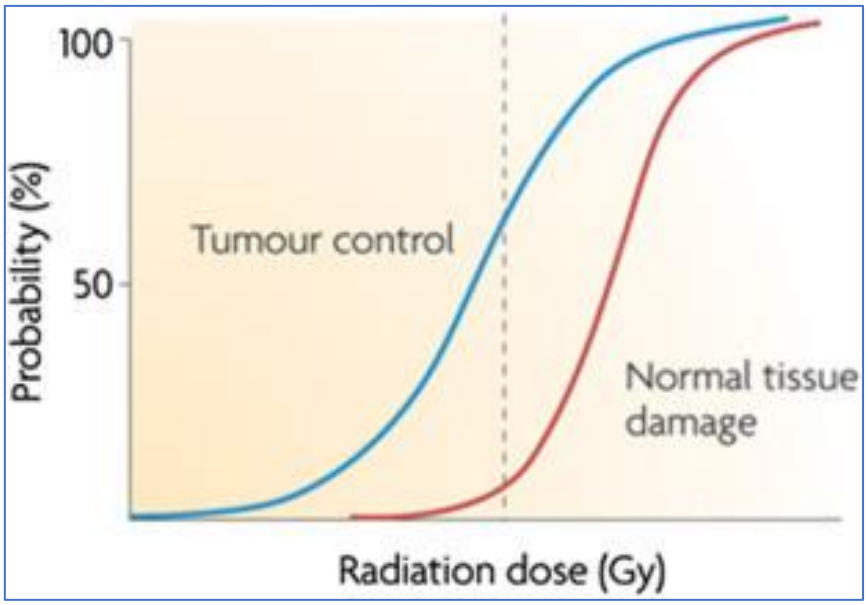

Figure 2-2: Tumour control probability vs normal tissue damage probability [16].

In the last 20 years advancements in radiotherapy technology including 4D CT scanning, inverse planning, multi-leaf collimation and on-board imaging have greatly improved the utility and accuracy of treatment by linear accelerator.

As a consequence the therapeutic ratio for many treatment sites has increased [17]. With the introduction of the multi-leaf collimator (MLC) and inverse planning treatment planning software it became possible to deliver a standard dose with far greater conformity. The improved conformity saw a marked improvement in clinical outcomes with normal tissue toxicities greatly reduced. Later with more precise linear accelerators and the use of on-board imaging treatment volume margins were reduced and fraction doses substantially increased. Stereotactic ablative body radiotherapy (SABR) or stereotactic body radiotherapy utilises dose escalation to deliver hypofractionation dose regimens. High doses (≥8 Gy) per fraction are delivered in a small number of fractions.

SABR has been demonstrated to achieve excellent local control rate for solid tumours with little metastatic disease. This treatment is considered most appropriate for sarcomas, colorectal cancer and germ cell tumours [18]. To ensure beams are delivered precisely radiotherapy clinics have introduced rigorous patient-specific quality assurance, high-performance machine credentialing as well as prescriptive treatment protocols that more greatly involve the radiation oncologist and the medical physicist.

2.5 Radioprotectors

While image guided patient positioning set up and VMAT dose delivery have improved the therapeutic ratio normal tissue toxicity remains a limiting factor in the treatment of many diseases using radiation therapy. The need to irradiate margins about a tumour and the proximity of critical structures to the treatment volume means normal tissue complication or toxicity must always be considered when deciding on a treatment option.

An alternative to reduce normal tissue toxicity is the use of radioprotectors, agents that when present prior to or shortly after radiation exposure alter the normal tissue response. To be useful in the radiotherapy clinic radioprotectors should ideally have the following characteristics:

- *Selective*. Protects normal tissue without protecting malignancy otherwise there will be no gain in the therapeutic ratio.
- *Easy to deliver and with minimal toxicity.* If the agent is to be delivered safely and precisely in conjunction with radiotherapy, then biological uptake and clearance and toxicity must be well known.
- *Protects the RIGHT normal tissue.* Prevents early or late toxicities that are dose limiting or significantly reduce the quality of life of the patient (i.e. mucositis, pneumonitis, myelopathy, xerostomia, proctitis and leukoencephalopathy).

As described previously in section 2.2 free radicals are responsible for about 2/3 of the damage inflicted by megavoltage photon radiation. Therefore, for an agent to protect tissue against primary free radical damage, the agent needs to be present at the time of exposure and in sufficient concentration to compete with free radicals produced through photon-tissue interaction. Superoxide dismutase (SOD), catalase, glutathione peroxidase, and glutathione reductase are examples of naturally occurring antioxidants that mitigate free radical - mediate damage within the cell [19]. General antioxidant protection is also provided by low molecular weight antioxidants, such as ascorbic acid, tocopherols, polyphenols, and thiols such as glutathione. These compounds neutralise oxidants by hydrogen atom donation [20]. Whereas radioprotectors need to have radical-scavenging properties and can also exert general antioxidant activity, all antioxidants cannot afford radioprotection [21].

This determination may be a result of the relative reactivity of radiation-induced reactive species compared with those generated under conditions of general oxidative stress (i.e., H_2O_2 exposure). Scavenging hydroxyl radicals, such as those formed with radiation-induced damage, may be accomplished by almost any unsaturated organic molecule or molecule capable of H atom donation. Although hydroxyl radicals can be scavenged with equal efficiency by both radioprotectors and antioxidants, cellular and in vivo radioprotection is observed only with radioprotectors. This suggests that a secondary species is generated by hydroxyl radicals and is responsible for critical target (i.e., DNA) damage. This less reactive secondary species may not be scavenged by conventional antioxidants either because they do not accumulate in proximity to the secondary radical or they may not have kinetic reactivity to scavenge them effectively. Thus, thiols such as Amifostine [22] and nitroxides [23] have sufficient reactivity to efficiently scavenge secondary radicals. Conversely, well-known antioxidants such as vitamin C and vitamin E do not act as classic radioprotectors.

For modern SABR a high dose fraction, small margins and delivery to a moving target leaves little room for error. In such cases a radioprotector drug or nanoparticle could be valued insurance against geometric miss. To date the only therapeutically approved radioprotector is Amifostine [24], [25]. Initially used to reduce toxicity of the chemotherapy drug, Cisplatin, it is now used to reduced moderate to severe xerostomia, mucositis and dysphagia in head and neck cancer patients. However, its broad clinical use has been stalled due to moderate/high side effects of nausea, emesis and hypertension in some patients [26].

2.6 Cerium oxide nanoparticles

Cerium oxide is a lanthanide metal oxide crystal with a broad range of applications including use as an oxygen sensor [27], a catalytic converter [28], [29], a fuel cell [30], an anti-oxidant [31]–[33] and a radioprotector [31], [34], [35]. Its atomic structure is cubic fluorite with one Ce^{4+} ion surrounded by eight O^{2-} ions to form the corner of a cube, with each O^{-2} ion co-ordinated to four Ce^{4+} ions as shown by the unit cell in Figure 2-3a. The unit cell is the smallest repeating unit of a crystal.

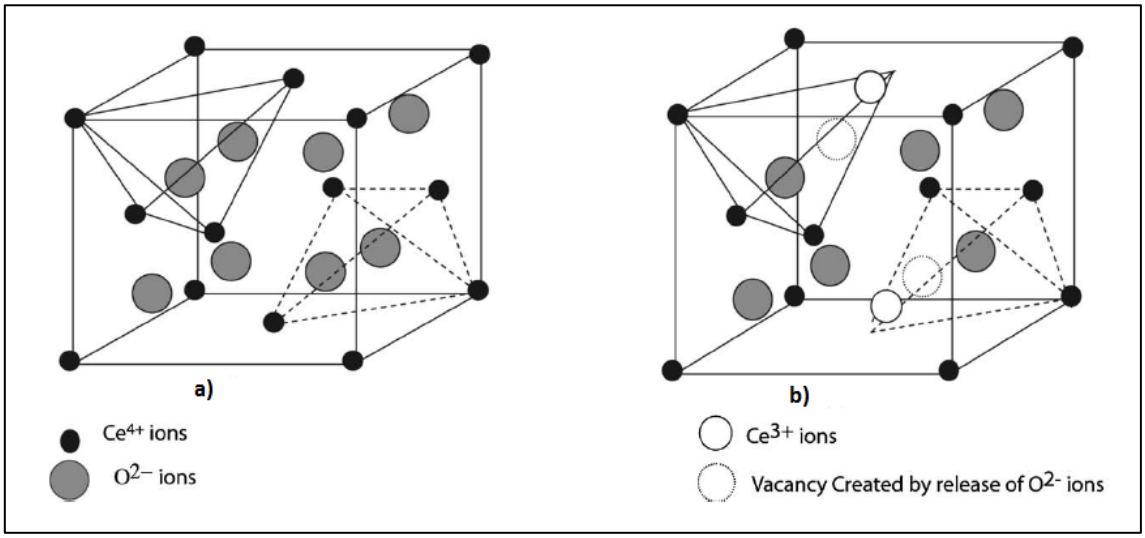

Figure 2-3: The unit cell of cerium oxide exhibits a cubic fluorite structure (a) which can be distorted (b) by oxygen vacancies within the lattice [36].

The symmetric nature of the cerium oxide unit cell allows its physical dimensions (x, y, z) to be described by a single lattice parameter, a. The lattice parameter for bulk cerium oxide is 5.410 Å or 0.5410 nm. The utility of the crystal is attributed to the ease at which cerium ions can switch between the 3+ and 4+ valence states at defect sites within the crystal. The oxidative switching is attributed to the similar energy of the 4f and 5d electronic states and the low potential barrier between them [37].

The oxygen vacancies that occur in at these defect sites allow easy passage of oxygen within the bulk material and the interaction of oxygen species about the surface of the crystal. When an oxygen vacancy occurs within the crystal a neighbouring cerium ion reduces to a 3+ valence state to affect electrostatic equilibrium. In the right conditions the redox potential of the cerium ions at the OVDs allow the facile cycling of valence states (3+⇨4+⇨3+) mentioned prior.

Cerium oxide nanoparticles can be made from a number of different synthesis methods; co-precipitation, spray-pyrolysis, hydrothermal [38] and sol-gel [39]. When cerium oxide nanoparticles are made small (< 20 nm) the strain within the lattice boosts the number of Ce^{3+} ions at the surface of the nanoparticle [40]. The efficacy of cerium oxide nanoparticles to work as a free radical scavenger has been shown to correlate with Ce^{3+} populations. While the exact pathways of reduction and oxidation are still under debate studies show that the scavenging is dependent on pH [41] and discriminates against tumour tissue owing to this pH dependence. Cerium oxide nanoparticles have been trialled in-vivo to mitigate normal tissue damage arising from the accumulation of free radicals. In one case Heckman et al. were able to penetrate the brain of mice with 3 nm cerium oxide NPs to reduce oxygen species levels and alleviate clinical symptoms and motor deficiencies in a murine model of multiple sclerosis. In another instance nanoparticle were taken up in the retina of mice and mitigated oxidative stress linked to retina disease. In both cases there was prolonged uptake of nanoparticles with no identifiable toxicity.

As a radioprotector, cerium oxide nanoparticles have been tested on a number of irradiated cell lines demonstrating an ability to mimic other antioxidant macromolecules like super oxide dismutase and catalase to reduce normal tissue reaction.

More recently cerium oxide particles have been demonstrated through in-vivo experiments to decrease xerostomia and dermatitis in head and neck irradiation [42] and protect epithelial tissue in the lung and gut by scavenging free radicals and increasing the cellular concentration of SOD2 [43], [44].

Current work on cerium nanoparticles looks to optimise colloidal stability, uptake and serum clearance through to tissues and organs. It's widely believed that these outcomes are best achieved through the use of biocompatible coatings such as folic acid or acetate/EDTA. While most results to date have been promising there are some reports of toxicity that must be further investigated and work is now underway to better understand the internalisation and subcellular localisation of cerium oxide nanoparticles within individual cell types [45].

Chapter 3

METHODS and MATERIALS

3.1 Cerium oxide particle synthesis

Cerium oxide particles were synthesised and characterised at the Institute of Superconducting and Electronic Materials (ISEM), University of Wollongong under the supervision of Associate Professor Konstantin Konstantinov and the assistance of postgraduate students Dean Cardillo and Kathrin Bogusz. Two methods of synthesis were used to produce cerium oxide and iron (Fe^{3+}) doped cerium oxide particles. The first method chosen was co-precipitation, however due to later complications it was succeeded by spray pyrolysis. Iron (III) was chosen instead of samarium to dope particles as it was readily available and also trivalent. It was reasoned it should effectively suppress Ce^{3+} formation through lattice inclusion.

3.1.1 Synthesis by co-precipitation

Co-precipitation of cerium oxide particles, pure and doped, was achieved using cerium (III) nitrate hexahydrate $Ce(NO_3)_3.6H_2O$ (Sigma >99%), iron (III) nitrate nonahydrate $Fe(NO_3)_3.9H_2O$ (Sigma >99%) and anhydrous sodium hydroxide *NaOH* (Sigma > 99%). 8.68 g of $Ce(NO_3)_3.6H_2O$ (0.02 moles) and 2.81 g of *NaOH* (0.07 moles) were added to separate beakers containing 100 ml of deionised water. Under magnetic stirring the $Ce(NO_3)_3$ solution was added drop wise to *NaOH* at a rate of 5 ml/min. The resulting purple suspension was centrifuged (Eppendorf, Centrifuge 5702) at 1100 rpm for 10 minutes. The solution was decanted and the resulting purple precipitate muddled with glass rod and deionised water to produce a suspension. Centrifuge and wash was repeated twice with a final centrifuge.

The precipitate was dried at 60 °C for 12 hours becoming a grainy powder of cerium oxide particles. A portion of powder was placed in a ceramic crucible and heated in a tube furnace for 6 hours at 300 °C with the intent of dehydrating, purifying and crystallising. The synthesis of the iron doped cerium oxide particles occurred similarly except moles of Fe^{3+} ions were substituted for moles of Ce^{3+} ions to achieve the successive atomic doping of 5 %, 10 % and 20 % iron as shown in Table 3-1.

Cerium Oxide Particles	Reagents dissolved in DI water
Pure	*0.02 moles Ce^{3+} + 0.07 moles NaOH*
5 % Fe	*0.019 moles Ce^{3+} + 0.001 moles Fe^{3+} + 0.07 moles NaOH*
10 % Fe	*0.018 moles Ce^{3+} + 0.002 moles Fe^{3+} + 0.07 moles NaOH*
20 % Fe	*0.016 moles Ce^{3+} + 0.004 moles Fe^{3+} + 0.07 moles NaOH*

Table 3-1: Reagent quantities for synthesis of nanocrystalline cerium oxide particles by co-precipitation

3.1.2 Synthesis by spray pyrolysis

The second synthesis method of spray pyrolysis did not require *NaOH* to form cerium oxide particles, however to reduce environmental contamination nitrate quantities had to be increased by a factor of 10. For cerium oxide particles 450 ml of 0.5 M cerium (III) nitrate solution was sprayed, via a peristaltic pump, through a nitrogen pressured aerosol head at a rate of 300 ml/hr into a tube furnace standing vertically at ~3 m tall. The heat of the furnace rapidly reacted the cerium (III) nitrate solution with air to form spherical cerium oxide particles [46]. The particles fell to the base of the furnace and were forced by air into a catcher bin.

After 100 ml of the cerium (III) nitrate solution had been sprayed the delivery system was stopped and the catcher bin cleaned and emptied. The cerium oxide particles removed were kept but not used as to avoid contamination from previous material works. The system was restarted and the remainder of the viable cerium oxide particles were collected. This process was repeated for all iron doped particles. Again, as was the case previously iron doping was achieved through molar substitution of Ce^{3+} for Fe^{3+} ions. It took approximately two days to produce the pure cerium oxide and the 5%, 10% and 20% iron doped cerium oxide powders. Quantities of all reagents used in synthesis can be found in Table 3-2.

Cerium Oxide Particles	Reagents dissolved in DI water
Pure	*0.2 moles Ce^{3+}*
5% Fe	*0.19 moles Ce^{3+} + 0.01 moles Fe^{3+}*
10% Fe	*0.18 moles Ce^{3+} + 0.02 moles Fe^{3+}*
20% Fe	*0.16 moles Ce^{3+} + 0.04 moles Fe^{3+}*

Table 3-2: Reagent quantities for synthesis of nanocrystalline cerium oxide particles

3.2 Particle characterisation

3.2.1 X-ray diffraction

Crystal structure analysis was performed on all particles, co-precipitate and spray pyrolysis, using a GBC Mini Materials Analyser (MMA) X-ray Diffractometer. Mortar and pestle and 100% ethanol was used to break up particles and produce a slurry. This slurry was applied to a quartz plate evenly ad after evaporation produce a thin mono-layer as show in Figure 3-1.

The mono-layer was irradiated with a monochromatic, copper K_α x-ray beam (λ = 1.5406 Å) from 20 - 90° with a step size of 0.02° and a speed of 2°/min. Traces software was used to identify the nature of the phase. The Scherer formula below was applied to the most intense 3 peaks, which were fitted using a Gaussian function, to determine the mean crystallite size:

Equation 3-1

$$\overline{T_c} = \frac{k\lambda}{B.cos\theta} \qquad \text{where } B = B_{obs} - B_{std}$$

where $\overline{T_c}$ is the mean crystallite size, k is a constant shape factor for cubic crystals set at 0.85, λ is the measuring x-ray wavelength, B_{obs} is the observed full width half maximum (FWHM) of the measured peak, B_{std} is the instrumental contribution and ϑ is the diffracting angle of the chosen peak. Unit cell parameters and phase composition were investigated using Rietveld refinement (MAUD software) utilising bulk phase files for cerium oxide (#01-089-8436 from ICSD) and haematite (#13-0534 from JCPDS).

Figure 3-1: XRD prepared slurries for pure (right) and 5% iron doped (left) cerium oxide particles.

3.2.2 Thermal gravimetric analysis

Thermo-gravimetric analysis (TGA) using the Metter Toledo TGA/DSC STAResystem was used to determine the optimum annealing temperature. 100 mg of particles were placed in an aluminium oxide crucible. The crucible and a standard crucible were placed in an argon atmosphere and heated from 60 ^{o}C to 1000 ^{o}C at a rate of 10 ^{o}C/min. The weight of both the standard and sample crucible was tracked to determine an approximate annealing temperature. Purity was assessed as a function of percentage weight loss. When weight loss ceased the sample was considered pure and the heating temperature noted as an approximate of the optimum annealing temperature. The maximum heating temperature was well below the melting and boiling point of cerium oxide lattice being 2,400 ^{o}C and 3,500 ^{o}C respectively.

The temperature derived from this process would be higher than optimal due to the lag of thermal equilibrium; it takes time for heat to propagate throughout the material. The optimum annealing temperature determined by heating the particle powders at progressively hotter to find the minimum temperature at which weight loss plateaued.

3.2.3 Optical emission spectroscopy

The atomic concentration of cerium and iron ions within pure and doped cerium oxide particles was assessed using inductively coupled plasma - optical emission spectrophotometer (ICP-OES). The ICP-OES used at ISEM is the Vista MPX by Aligent. Standards solutions were fed into an argon torch where ions of interest omitted characteristic light. Standards curves were constructed to calibrate light intensity to concentration of ions of interest. 1000 ppm standard solutions for cerium and iron were purchased from Aligent. Using serial dilution standard curves were produced ranging from 0 - 120 ppm. These curves were used to convert light output for sample solutions into constituent atomic concentrations.

To overcome strong covalent bonding of the ceramic particles sample solutions were prepared using 50 % hydrogen peroxide H_2O_2 (Sigma) and 35 % nitric acid HNO_3 (Sigma). To dissolve the pure cerium oxide particles 5mg of particle powder was added to 5 ml of nitric acid and lightly stirred at 60 ^{o}C in a fume hood. Hydrogen peroxide was then added drop wise until the suspension turned clear (3-5 drops), giving approximately 500 ppm cerium solution. 1 ml of the cerium solution was pipeted into a 10 ml volumetric flask and 9 ml of 18 MΩ deionised water added to make a 50 ppm solution. This digestion process was repeated for all particle powders.

3.2.4 Transmission electron microscopy

Images of the particles were acquired to investigate crystallite size and particle size. Transmitted electron detector (TED) images were taken using a JSM-7500FA cold Field Emission Gun Scanning Electron Microscope (JEOL, Japan). The microscope was operated at an accelerating voltage of 17-25 kV at a working distance of 8 mm and a beam current of 10 µA with a spot size setting of 8. Particles were sonicated in 100 % ethanol at a concentration of 1000 µg/ml. The resulting suspension was pipeted on to carbon film coated copper grids and left to dry.

3.2.5 X-ray photoelectron spectroscopy

X-ray photoelectron spectroscopy was utilised to determine the populating ratio of Ce^{3+}/Ce^{4+} ions within the pure and iron doped cerium oxide particles. The analyser was installed in a high vacuum chamber with a base pressure below 8-10 millibars. X-ray excitation was provided by aluminium K_α photons with energy of 1486.6 eV at a voltage of 12 kV and a power of 120 W. The spectra were collected at a pass energy of 20 eV in a fixed transmission mode. The spectra were calibrated using the C1s carbon binding energy peak found at 284.8 eV.

The peak represents the C-C bond found in adventitious carbon; a common contaminate introduced via the atmosphere during sample preparation. Peak binding energy parameters for the cerium binding spectra were collected from the N.I.S.T photoelectron spectroscopy database [47] and are shown in Table 3-3. The data was used to deconvolve the 11 orbital peaks found in cerium oxide NPs as a result of oxygen defects.

Peak	Ion	Intensity (a.u)	Position (± eV)	Electron orbital
A	Ce^{4+}	Std	916.7	$3d_{3/2}$
B		Std	907.3	$3d_{3/2}$
C		Std	900.8	$3d_{3/2}$
D		A*1.5	898.3	$3d_{5/2}$
E		B*1.5	888.6	$3d_{5/2}$
F		C*1.5	882.3	$3d_{5/2}$
G	Ce^{3+}	Std	903.7	$3d_{3/2}$
H		H*0.85	899.1	$3d_{3/2}$
I		Std	855.4	$3d_{3/2}$
J		I*0.85	855.4	$3d_{3/2}$

Table 3-3: Binding energy peak data for cerium oxide retrieved from N.I.S.T XPS database.

3.3 Cerium oxide particle storage and preparation

3.3.1 Storage

As a precaution, it is suggested anyone handling the particles use nitrile gloves and a micron gauge facemask in a well-ventilated area. Pure cerium oxide particles were found to be extremely hygroscopic. Particle powder (16 - 20 g) was kept in a 10 L vacuum desiccator at ISEM, Innovation campus. Working stock used entirely at IHMRI was kept in autosampler vials buried in 3 mm silicon dioxide beads (Sigma Aldrich) held within a small plastic container (Figure 3-2).

This allowed the particles to be moved about IHMRI easily. All particles were handled using a small trough spatula and gloves. Weighing of particles was done in a still space to prevent powder being blown away. To extract the particles, the autosampler vial was rotated while dragging the spatula through the top layer of the powder. When there was sufficient material the spatula was pressed against the side of the vial to compress the powder. The pressing further reduced particle loss.

Figure 3-2: Portable desiccator for transport of cerium oxide nanocrystalline particles

3.3.2 Weighing and sterilising

The particles were weighed using the precision balance (KERN, ALS 220-4N). Prior to weighing the balance was levelled using the inbuilt spirit level. A mount was fixed by adhesive plasticine to the centre of the balance to ensure the sample tube (Falcon 15 ml, Sigma Aldrich) stayed upright when particles are being weighed. The uncapped tube was placed in the balance, all doors closed and the tube given time to settle. The tube weight was tared. The tube was carefully removed from the balance and 3-4 mg of particles placed swiftly at the bottom of the tube and the tube given a quick tap with the spatula.

It's important all particles get to the bottom of the tube to avoid weighing error. The tube was returned to the balance, all doors again closed and the particle powder weight recorded. Ideally particles should be placed in the falcon tube just once. It takes a little practice to be able to visually determine the weight of the particles; especially as density changes significantly between pure and doped cerium oxide powders. Particles were then sterilised using an autoclave on dry cycle at 121 ^{o}C for 15 minutes at 2 bars of pressure. Before sterilising tubes were places in a 500 ml beaker and their lids screwed open to allow for pressure equalisation during the drying phase. The lids were tightened immediately after the end of the cycle to prevent contamination.

3.3.3 Nanoparticle formation using sonication

Sonication was essential for the cellular activity of cerium oxide particles as micron size nanocrystalline CeOx spheres were broken down to nano size fragments. Inside the BSC falcon tubes containing particles were filled with warm (37 ^{o}C) DPBS (- -) to produce 1000 µg/ml particle suspensions. The warm DPBS helped to keep cerium oxide particles dispersed during initial sonication. Capped falcon tubes were placed in the tube holder (orange) and fixed to sonication bath (Branson 3800) as shown in Figure 3-3. The bath was filled with tap water until the surface of all particle suspensions sat below the surface of the water fill. Suspensions were sonicated for 2 hours. Every 20 minutes suspensions were removed from the bath, shaken vigorously for 10 seconds and rotated clockwise to the next position to ensure consistent sonication.

When sonication was successful the suspensions became 'milky' and particles stay suspended for a minute or more (Figure 3-4). The density of the materials, while not quantified, is significantly higher than water. Coupled with an agglomerate size of at least 50nm in a single dimension means eventually all materials will gravitate to the bottom of the flask to form sediment.

Figure 3-3: Sonication of cerium and iron doped particle suspensions in PBS (- -). In later setup tube positions were spread evenly about the bath and tubes rotated though positions during sonication to optimise fracturing.

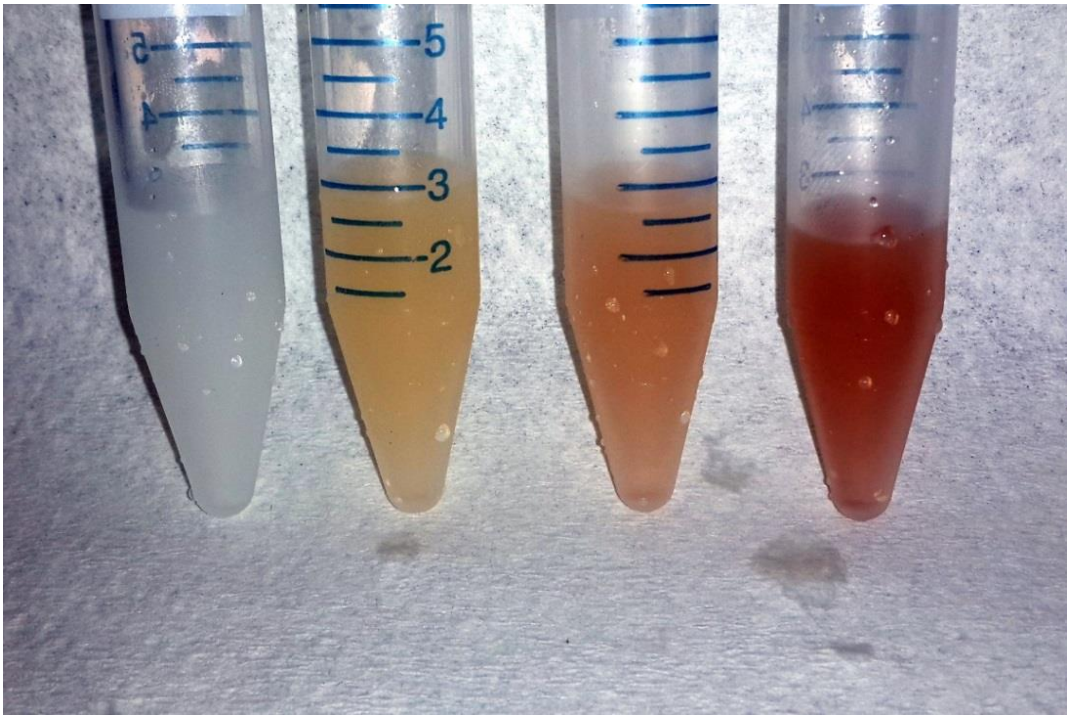

Figure 3-4: Suspensions of cerium oxide nanoparticles at 1000 µg/ml in PBS (- -) formed through sonication.

3.4 Biological assessment

Cell growth and radioprotection studies of cerium oxide nanoparticles were performed by clonogenic assay at the Illawarra Health Medical Institute (IHMRI) under the supervision of Dr Moeava Tehei. The 9L gliosarcoma cell line (ECCC, Salisbury, Wiltshire, UK) was chosen for all cell line studies. Although a cancer analog, previous work by Briggs (2013) had shown the 9L cell line to be selective to radioprotection by pure CeOx NPs undergoing megavoltage radiation exposure [48]. The doubling time of the cell line was approximately 36 hrs.

3.4.1 Cell culture reagents and consumables

A range of media, supplements and stains were required to maintain cell viability and assess the effects of particle inclusion. Materials used specifically for health and maintenance of the cell line were Dulbecco's Modified Eagle Media (DMEM), Fetal Bovine Serum (FBS), Penicillin-Streptomycin (Pen Strep), Dulbecco's Phosphate Buffered Saline (DPBS) and Trypsin EDTA. The DPBS came in two variants, with inclusion of calcium and magnesium labelled "+ +" and the omission of these ions labelled "- -". Calcium and magnesium ions promote cell adherence. All biological materials were handled in a class 2 Biological Safety Cabinet (BSC) and additives and equipment to be used within were sterilised by autoclave and/or ethanol spray before use.

3.4.2 Preparation of cell culture medium

DMEM is supplemented using 10% FBS and 1% Pen Strep to boost cell growth and fight infection. Fully supplemented DMEM is labelled c-DMEM for 'complete' media. To assess viability of the completed media 3 aliquots of 1 ml volume were drawn into 1.5 ml Eppendorf tubes and incubated at 37^{o}C in 5% (v/v) carbon dioxide atmosphere. Three days later the aliquots were assessed for microbial intrusion.

The chosen DMEM contains a pH indicator of phenyl red and is pH buffered through the inclusion of 3.7 g/L of sodium bicarbonate. The media is buffered for 10 % (v/v) CO_2 environment resulting in a slightly basic media when incubated at 5 % (v/v) carbon dioxide. Cell proliferation and the resulted output of carbon dioxide will reduce media pH towards neutral. The colour of the media is a helpful tool for quickly assessing cellular activity and in this case microbial intrusion as shown in Figure 3-5.

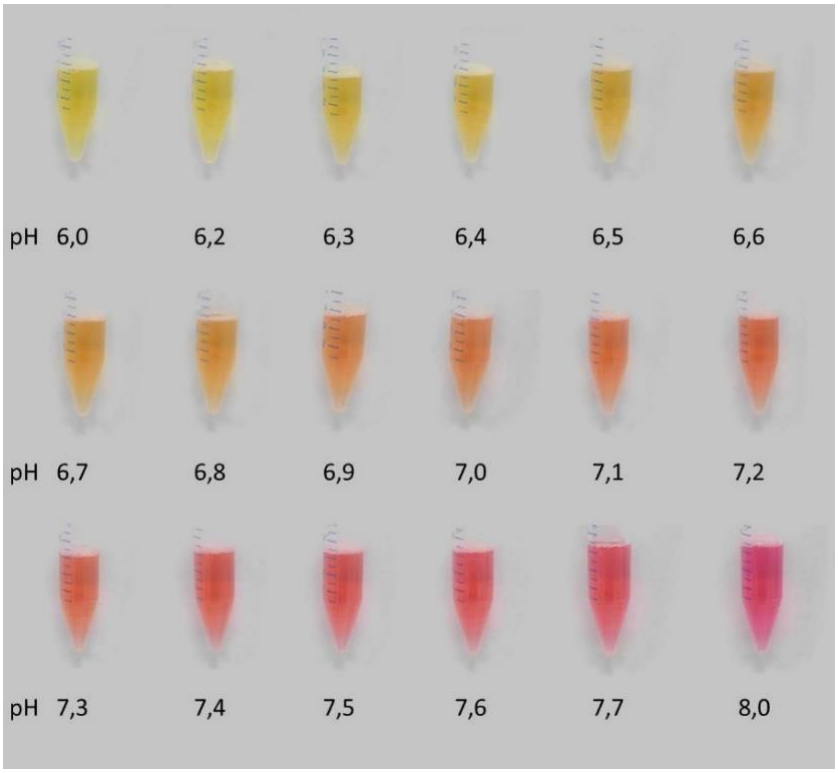

Figure 3-5: Phenyl Red as a pH indicator in DMEM cell line media.

3.4.3 Passaging (subculture) of cell line

Cells were grown as a monolayer in a T75 flask (75 cm^2), containing c-DMEM until they reach 90 % confluence. Cells were then passaged to a new flask to prevent cell degradation and change to morphology. Passaging occurred inside the BSC. Media was removed by pipet from the T75 flask and the monolayer washed with DPBS (- -) to remove cellular debris and possible contaminates. 2-3 ml of trypsin was then carefully added and the flask incubated for 3-7 minutes.

The purpose of trypsin is to detach the cells by dissolving surface protein anchors. Upon removal from the incubator the flask was gently tapped to remove attached cells. Media was observed at 10X magnification to verify detachment using a low powered inverting microscope (Olympus, KX series, 4-40X magnification). 8 ml of c-DMEM was added to the flask and the cell suspension was drawn and flushed 10 times, slowly, taking care not to aerate the media too greatly. The cell suspension was again viewed under the microscope to confirm all cells were separated and intact. 0.1 ml of cell suspension was then aliquoted into an Eppendorf tube and from this 10 µL was pipeted to a mixing palette and diluted at a range of 1:5 to 1:7 using Trypan Blue dye.

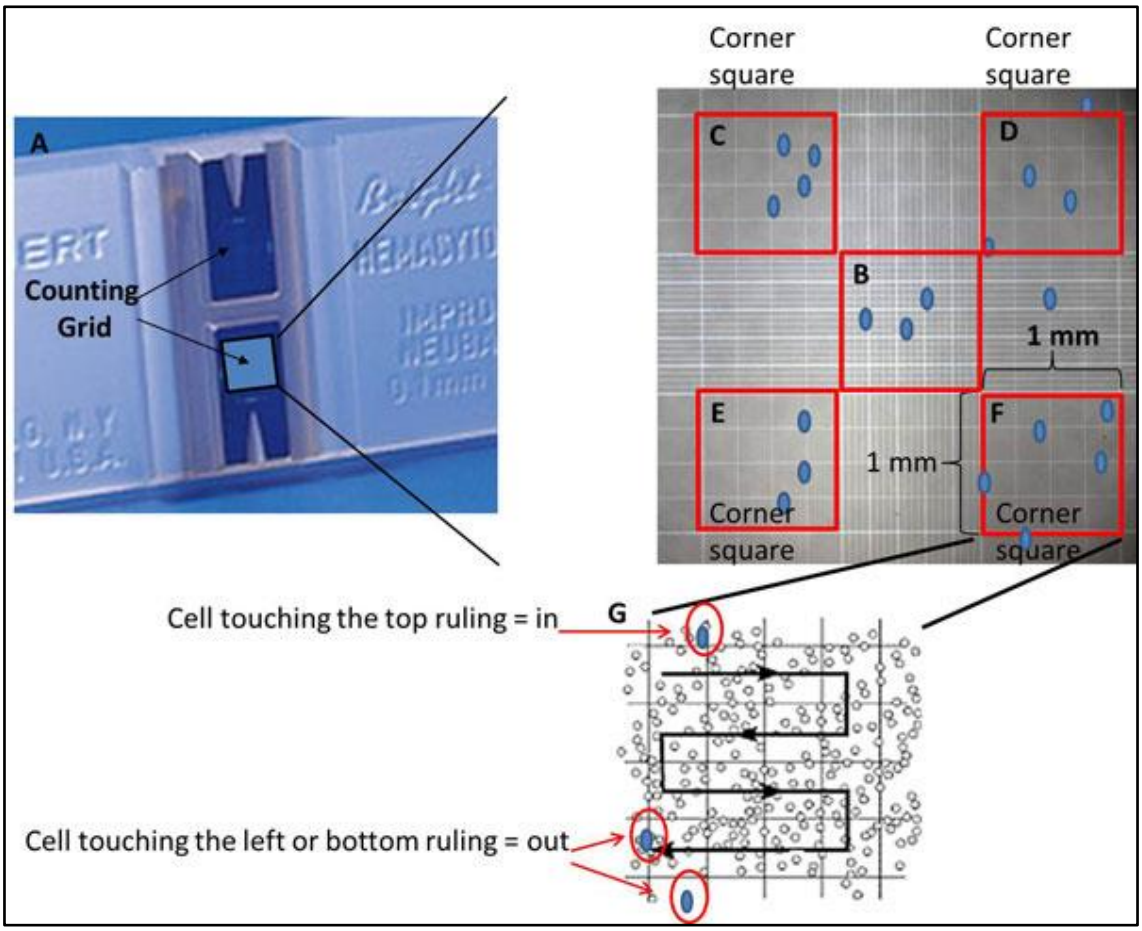

Figure 3-6: Counting viable cells using a haemocytometer [49].

The dye has two roles. It serves as a dispersant to spread cells evenly on the counting grid of the haemocytometer (Brand, Germany) so they don't overlap. Secondly, the diazo dye selectively penetrates the membrane of dead cells. When viewed under the inverting microscope at 20 X magnification the viable cells contrast well against the Trypan Blue background. The full grid on the haemocytometer contains nine squares, each of 1 mm^2 area and a depth of 0.1mm containing a volume of 100 nl. Cells are counted in 5 of these squares (marked red in Figure 3-6) to determine an average amount of cells per square. To ensure an accurate count cells on the left and bottom perimeter of each square are excluded. The cell concentration of the cell suspension in the T75 flask is then determined using the following formula:

Equation 3-2 $cells/ml = average\ cells\ per\ square * dilution\ factor * 10^4$

The cell concentration and Table 3-4 were then used to determine the cell suspension volume required for seeding. The cell suspension was transferred from the old T75 flask to new T75 flask containing 20 ml of fresh c-DMEM. Details of the cell type, user, passage number and date were written on the flask using indelible pen. The seeding populations in Table 3-4 have been determined experimentally and average over a wide range of passages (30 - 60). To ensure the health of the cell line doubling times were continually verified throughout the lifetime of the cell line.

Flask	Surface Area (cm^2)	90% confluence	3-day seeding	4-day seeding	5-day seeding
T12.5	12.5	1,200,000	300,000	200,000	120,000
T75	75	10,000,000	2,500,000	1,500,000	-

Table 3-4: Seeding population for 9L cells was determined through several lifetimes of the cell.

3.4.4 Clonogenic survival assay

In a clonogenic assay a cell's survival is correlated to a minimum size colony grown on the surface of a plating dish. The gold standard for this type of assessment is colonies of 50 cells or more grown for approximately 14 doubling times [50]. For the purpose of biological assessment, a cell is deemed dead when it can no longer proliferate. A surviving cell that can proliferate indefinitely is known as a clonogen.

9L clonogenic assays were perform on the pure and iron doped cerium oxide nanoparticles using T12.5 flask and BD 100 mm Primaria culture plates. The Primaria plates have a heat-treated surface that improves cell adherence. The seeding of culture plates is known as plating. 5 days prior to plating 120,000 cells were transferred to each T12.5 flask containing 5 ml of c-DMEM to achieve a surface cell density of 9,600 cells/cm^2. This density of cells achieved a 90% confluence at the time of plating.

1 day prior to plating particles were weighed, sterilised, sonicated and included in flasks. 250 µL of 1000 ug/ml nanoparticle solution was added to required T12.5 flasks to achieve a particle concentration of 50 ug/ml. Flasks were then stored in incubator at 37 ^oC in 5% (v/v) CO_2 environment. Before plating occurred, equipment was sterilised and set up as shown in Figure 3-7. Once all equipment and materials had been included in the BSC, plates were labelled and filled with 10 ml of c-DMEM. Flasks were processed two at a time. For each flask media was removed and the cell monolayer washed with DPBS (- -). The layer was trypsinated and incubated to detach and separate the cell layer from the flask surface.

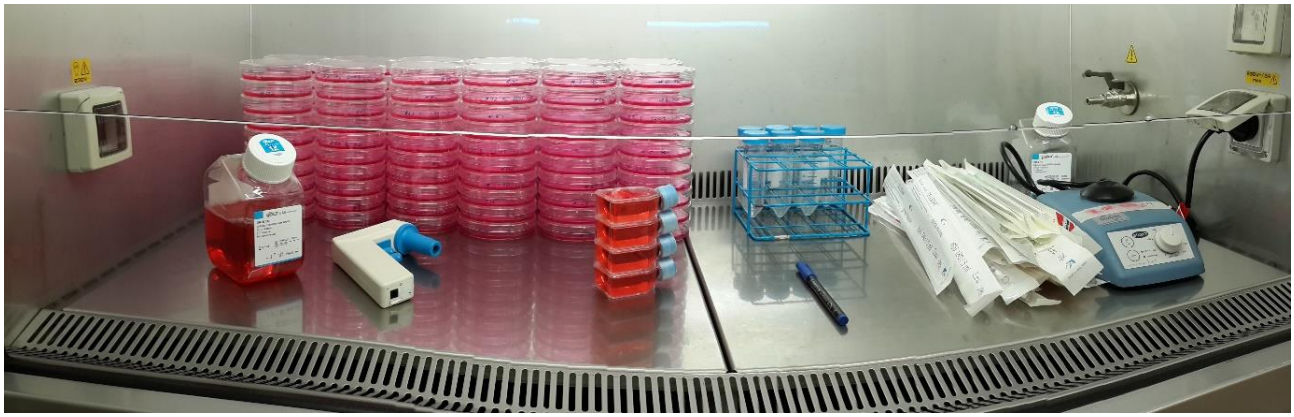

Figure 3-7: Preparation for 9L cell plating within the BSC requires the prefilling of many 100 mm plating dishes.

During incubation, a 50 ml conical tube was filled with 2.1 ml of c-DMEM. The flask was removed from the incubator and lightly tapped with cells being viewed at magnification to ensure they were not clustered or attached. 1 ml of c-DMEM was then added to the T12.5 flask and the cell suspension and fresh media drawn and flushed 20 times to separate cells. While separation is essential for clonogenic assays care should be taken not to overly aerate the media as too much oxygen can kill the cells. 0.3 ml of mixed cell suspension was drawn from the T12.5 flask and passed to the falcon tube to form a 1:8 diluted cell suspension. To ensure homogeneity the cell suspension was drawn and flushed 10 times. The conical tube was then centrifuged at 1200 rpm for 3 seconds and two 10 µL portions were micro-pipeted to the haemocytometer.

Equation 3-2 was used to determine the required seeding volumes for plating. Plates were moved back and forth in a consistent fashion to disperse cells evenly. When this process was completed for both flasks all plates were stacked and moved to the incubator. Plates were triplicated at seed counts of N, 2N and 4N to minimise sampling error and safe guard against fluctuations in cell growth (factors: adherence, doubling time, apoptosis, etc.). Plates were incubated for 21 days (approx. 14 doubling events) and afterwards colonies were fixed and stained for subsequent quantification.

Optimised cell seeding, based on inclusion effects should result in growth of 100-150 colonies. Below 100 colonies and the plate data start to become unreliable. Plates were first removed from the incubator and media was removed by pipet. Plates were washed twice with DPBS (+ +) to improve cell adherence. 1 ml of 75 % ethanol: 25 % crystal violet solution was added to each plate for a couple of minutes to stain and fix the colonies (Figure 3-8). The plates were rinsed with tap water until no residual crystal violet could be seen and left to dry for a few days. Crystal violet is considered a carcinogen and at the end of its use it was collected into a plastic jerry can for later disposal as a hazardous waste.

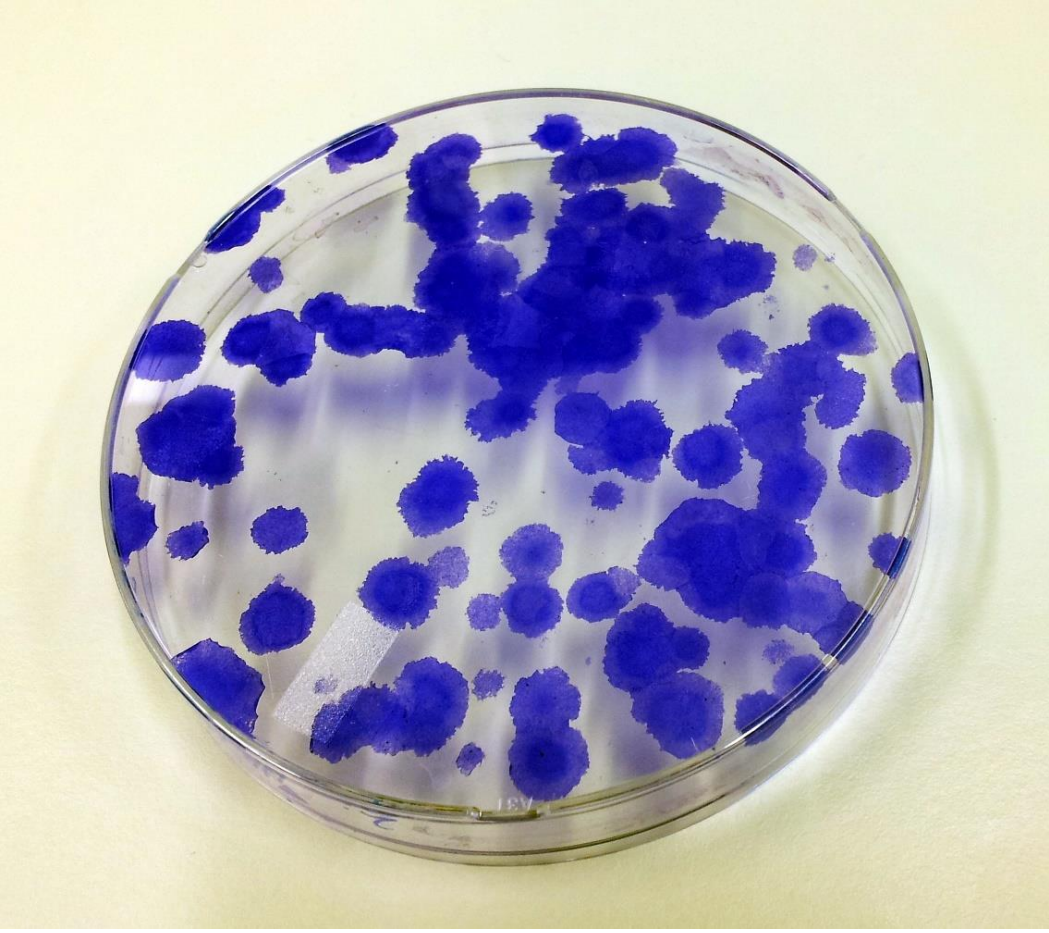

Figure 3-8: Stained colonies fixed with crystal violet.

Once dry plates were counted blind to determine the number of viable colonies present. Any colony containing 50 or more cells of a normal shape is considered viable. As some colonies can be quite small a stereoscopic microscope must be used periodically to verify colony sizes. Colony counts were then used to determine plating efficiency.

Equation 3-3 *Plating efficiency (PE) = no. of viable colonies / no. of seed cells*

Plating efficiencies for cell line series 9L + NPs were then normalised against the 9L control line series to determine survival/growth fractions.

3.4.5 Radiation delivery

Prior to irradiation at Prince of Wales hospital 9L cells were prepared as described in section 3.4.4. In addition, all T12.5 flasks were filled to the brim with HBSS with phenyl red inside the BSC. This was done to provide enough depth of build-up to ensure an accurate absorbed dose was delivered to the monolayer of cells. To ensure no contamination to the hospital environment all flask caps were wrapped with para-film and secured in a biohazard carry case for transportation to and from the hospital.

Cells were irradiated with the assistance of Deputy Director of Radiation Oncology Medical Physics, Dr Stephanie Corde. 10MV x-ray irradiation of cells was performed using an ELEKTA Versa HD linear accelerator (Figure 3-9). Four flasks at a time were placed on 10 cm of solid water (Model 457, Gammex) and secured with Superflab and solid water offcuts. The SSD was set to 100 cm and radiation was delivered using a 15 cm square field at a dose rate of approximately 500 Gy/min at the cell mono-layer.

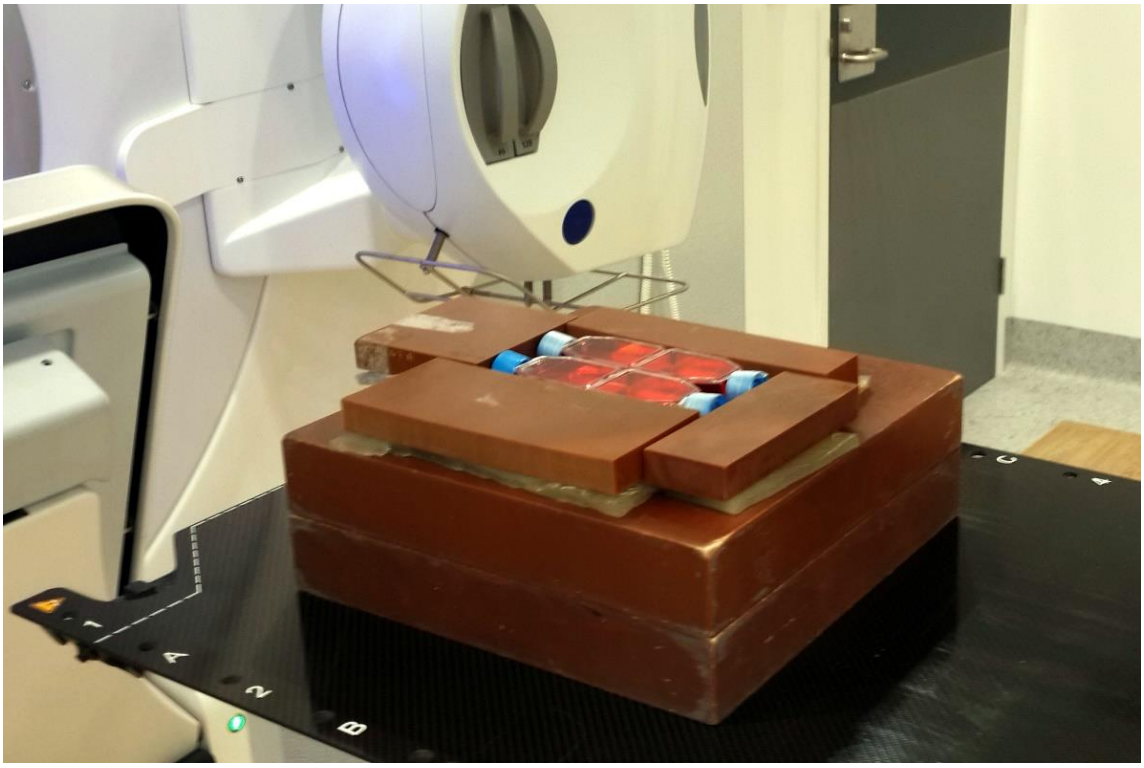

Figure 3-9: Flasks set for delivery of dose using the ELEKTA Versa HD linac.

To ensure accurate cell survival curves flasks were dosed to 1 Gy, 2 Gy, 3 Gy, 5 Gy and 8 Gy. In total seven flasks, including two control flasks were irradiated to obtain a single curve:

- 9L cells
- 9L cells + pure CeOx NPs
- 9L cells + 5% Fe doped CeOx NPs
- 9L cells + 10% Fe doped CeOx NPs

Upon return to IHMRI facilities flasks were immediately plated as described in section 3.4.4. Control flasks were plated first and last to mitigate cell growth during plating. Cells were again incubated for 21 days for a later stain and fix of grown colonies.

3.4.6 Cell survival curves

A survival curve describes the relationship between the radiation dose and the fraction of cells that survive. Survival curves for mammalian cells are normal presented with dose plotted linear on the horizontal axis and survival fraction plotted logarithmically on the vertical axis. They are an effective mechanism for characterising mammalian cell lines, comparing the effectiveness of different radiation therapies and concurrent drug schemes.

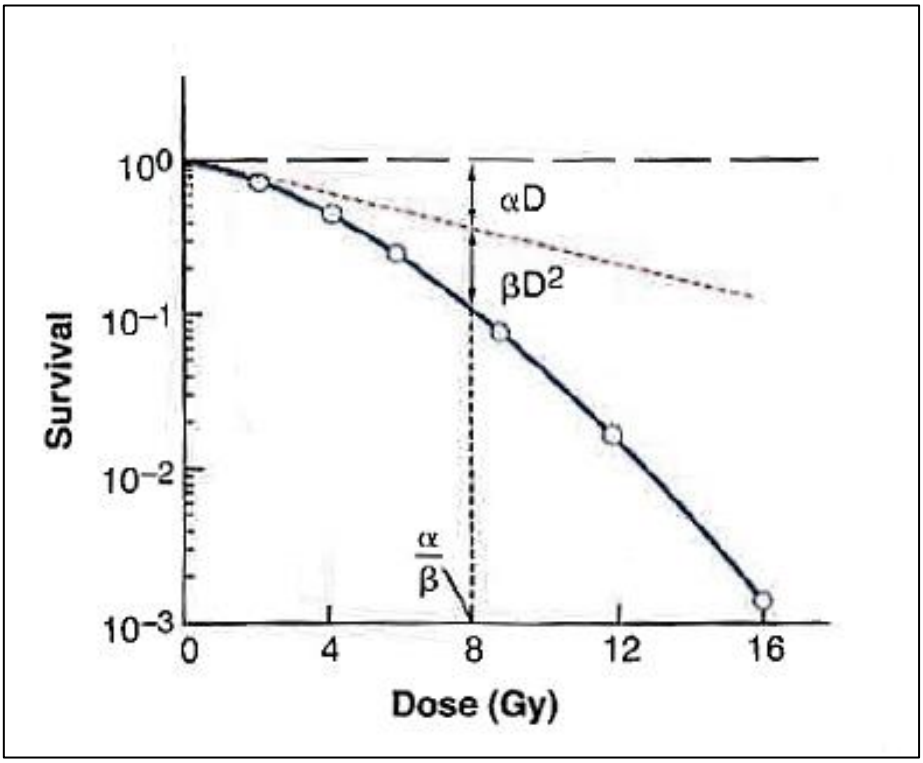

Figure 3-10: Survival curve for low LET photons. (Adapted from Hall 2012)

The intention in this study was to use survival curves to assess the impact of Ce^{3+} ion population on radioprotection afforded to the 9L cell line. The standard of comparison between curves was the Performance Enhancement Ratio (PER). The PER is the ratio of doses delivered for a common biological end point. In this instance 10% survival fraction (Equation 3-4).

Equation 3-4

$$PER = \left(\frac{Dose\ delivered\ to\ 9L+NP}{Dose\ delivered\ to\ 9L}\right)_{10\%\ SF}$$

Equation 3-5

$$Survival\ Fraction\ (S) = \exp(-\alpha D - \beta D^2)$$

The model of cell survival used in this study was the linear-quadratic model. It assumes two components to cell killing. One component, α is proportional to dose, *D* (a single hit kill) and the other, β the square of the dose (a double hit kill). By the fitting Equation 3-5 to each curve the radiosensitivity for each cell line series could be quantified as an alpha-beta ratio. This ratio can be used to characterise the radiosensitivity of the cell and better understand NP influence during radiation exposure. Generally, a radioresistant tissue would have a low α/β of 1-4 and a radiosensitive tissue would have a value much closer to 10.

Chapter 4

Results and Discussion

4.1 Cerium oxide particles by co-precipitation

4.1.1 Synthesis

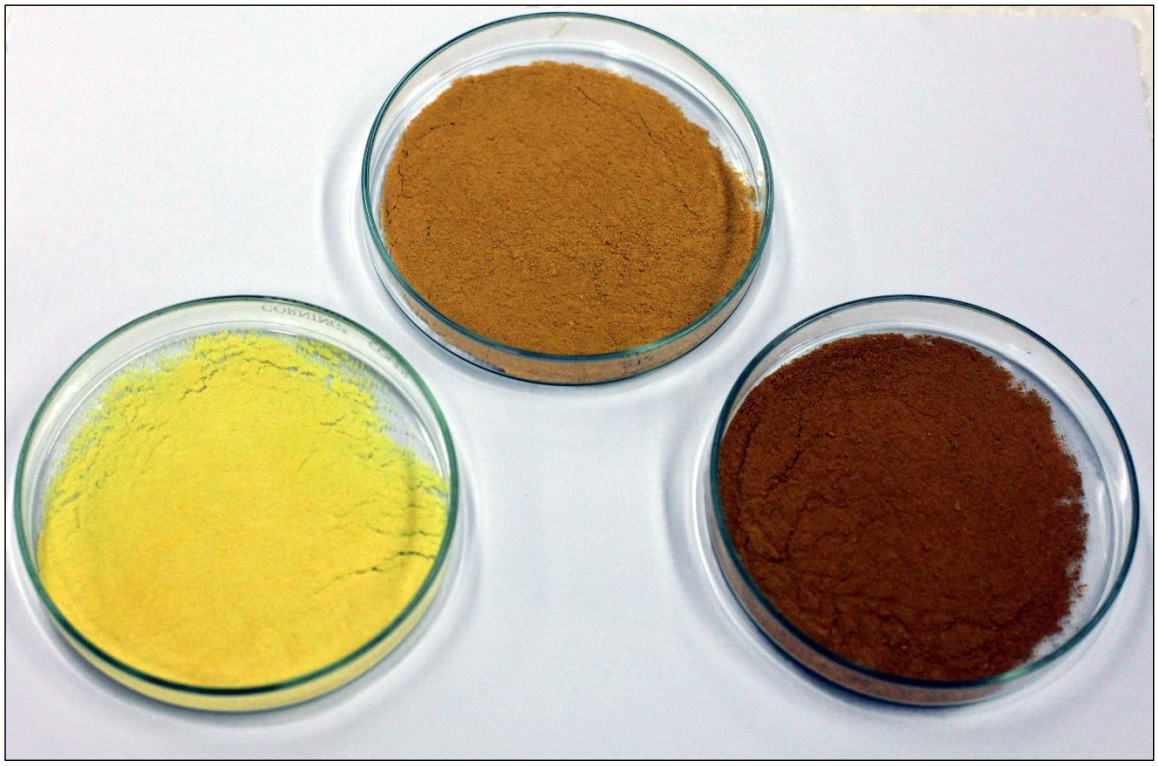

Figure 4-1: Cerium oxide powders formed by co-precipitation: pure, 5% iron and 10% iron doped and annealed at 550 °C

Producing small (<*10nm)* nanocrystalline cerium oxide particles by co-precipitation proved problematic. The main obstacle faced was the lack of detail in many methods published; temperature of solution, gestation time, concentration of oxidiser, etc. The chemical pathway of cerium oxide crystallisation can be ideally described by the following net chemical reactions:

Equation 4-1 $$Ce^{3+} + 3OH^{-} \rightarrow Ce(OH)_3$$

Equation 4-2 $$2Ce(OH)_3 + O_2 \rightarrow 2Ce(OH)_4$$

Equation 4-3 $$Ce(OH)_4 \rightarrow 2H_2O + CeO_2$$

Driven by strong basic conditions, *pH=8*, cerium nitrate reacted quickly to form a purple precipitate of cerium (III) hydroxide (Equation 4-1). The precipitate was muddled and washed to remove sodium and nitrates. An adverse effect of this process was the formation of a small portion of cerium nitrate, seen as a thin layer of white at the bottom of centrifuged mass. The precipitate was dried at 60 °C for 24 hours. Within a few hours of drying the precipitate had started to turn orange/ yellow as it oxidised (Equation 4-2) and crystallised, through dehydration (Equation 4-3). After 24 hours, the resultant product was a grainy yellow powder of cerium oxide nanocrystalline particles. In the case of the doped production more iron in the starting solution resulted in browner precipitates and browner cerium particles. The increasing depth of colour was an indication the doping process had been successful. (Figure 4-1)

4.1.2 Annealing

Nitrates are considered toxic to mammalian cells [51] and while small crystals were essential for the radioprotection efficacy of cerium oxide nanoparticles it could not be at the expense of purity. Annealing the particles thermally decomposed nitrates and drove further crystallisation. TGA was used as an expedient method of determining the lowest possible annealing temperature required to achieve purity within particle powder. After accounting for thermal equilibrium lag that temperature was determined to be approximately 700 °C for both cerium oxide particles and 10 % iron doped cerium particles (Figure 4-2), Weight loss of cerium oxide powder to the 10 % iron doped powder was 9 % to 7 % respectively. The larger weight loss of the pure particles is attributed to greater moisture content. Throughout experiments cerium oxide powder was found to be significantly more hygroscopic than its iron doped variants.

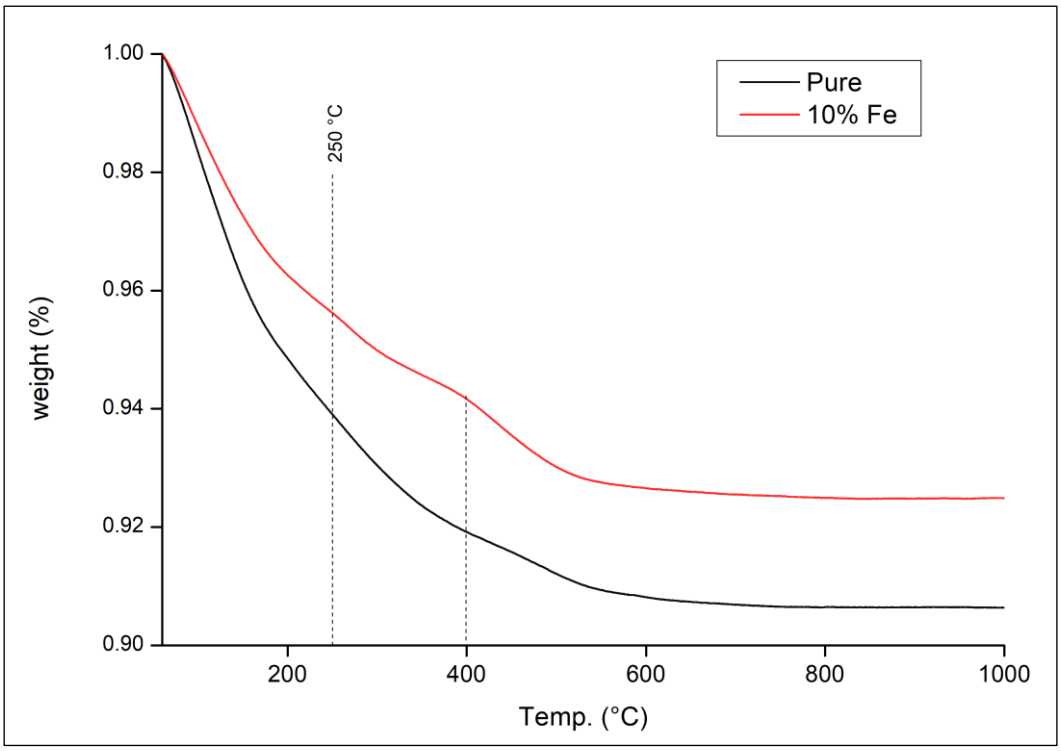

Figure 4-2: Ramp heating particles to determine gross annealing temperature of pure cerium oxide and 10% iron doped particles

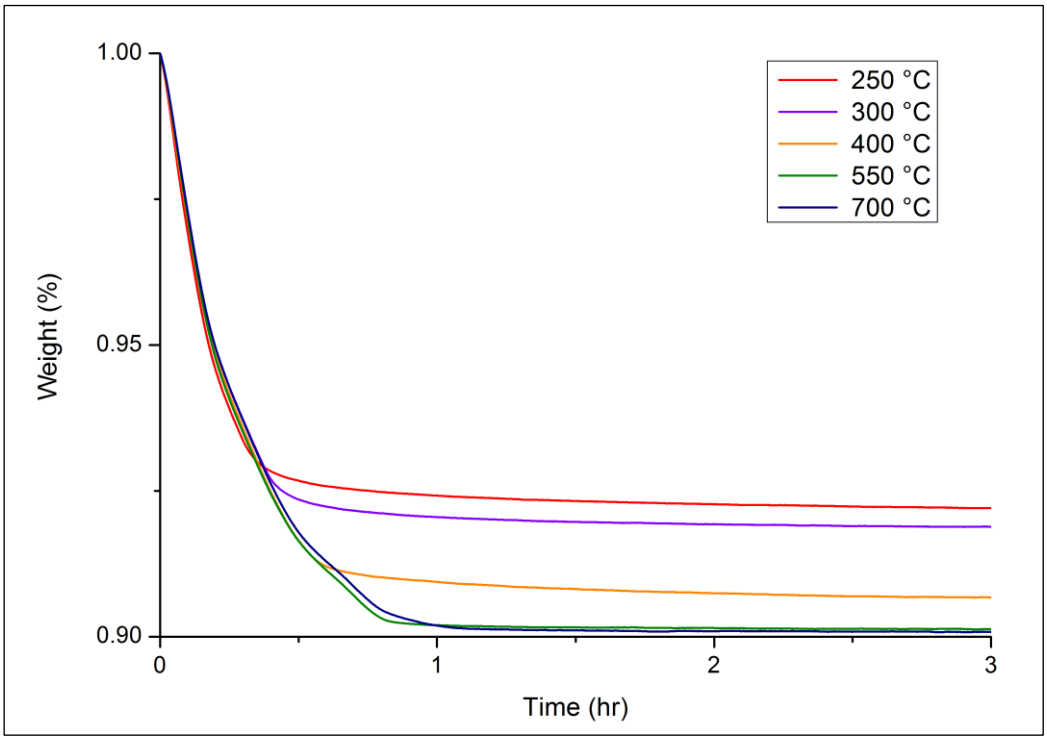

Figure 4-3: Step heating to determine precise annealing temperature for pure cerium oxide particles for controlled annealing of all particles.

Looking to Figure 4-2 the initial decay of mass in both mass curves (<250 ^{o}C) can be primarily attributed to water loss and the final decay (> 400 ^{o}C) largely to the crystallisation of amorphous cerium oxide and exotics *CeOOH* through dehydration. The intermediate decay curve (250 - 400 ^{o}C) of the iron doped mass curve can be attributed to thermal decomposition of iron nitrates and the crystallisation of amorphous iron oxide and exotics *FeOOH* [52]. The lowest temperature required to stabilise mass loss was found to be 550 ^{o}C (Figure 4-3).

4.1.3 Characterisation

When initially deciding on an annealing temperature TGA had not been available so it was decided to attempt a range of temperatures with the express purpose of producing a pure and small crystal. While a small crystal size was achieved at low heat it was later acknowledge that possible contamination by adventitious carbon would require annealing temperatures in excess of 500 ^{o}C to achieve the required purity. After TGA the required annealing temperature to was confirm to be 550 ^{o}C. XRD analysis determined all particles to be of a single cubic fluorite phase with the reflection pattern identified as that of cerium oxide.

XRD analysis of all annealed particles is presented in Table 4-1. For ease of analysis XRD patterns are displayed only for those particles annealed at 550 ^{o}C (Figure 4-5). The trending shown in these XRD patterns are similar for all three annealing sets; 60 ^{o}C, 300 ^{o}C and 550 ^{o}C. While a bulk cerium oxide crystal would display discrete peaks at each reflection angle the peaks of the cerium oxide particles were much broader suggesting small crystallite size. The Scherrer formula determined constituent crystal sizes for each particle to range between 3 nm and 15 nm.

Particle	Atomic composition by EDX			Anneal (°C)	Crystallite size (nm)	a (Å)
	Ce (%)	Fe (%)	Na (%)			
Pure	95 ± 2.0	0.0 ± 0.0	5.0 ± 2.0	60	3 – 4	5.436
				300	5 – 6	5.428
				550	14 – 15	5.416
5% Fe	91.8 ± 0.6	3.0 ± 0.2	5.2 ± 0.6	60	5 – 6	5.424
				300	6 – 7	5.419
				550	8 – 9	5.407
10% Fe	86.0 ± 4.0	7.7 ± 0.1	6.0 ± 4.0	60	6 – 7	5.417
				300	6 – 7	5.408
				550	8 – 9	5.399
20 % Fe	79.0 ± 4.0	17.0 ± 1.0	3.0 ± 3.0	60	4 - 5	5.414
				300	4 – 6	5.393
				550	6 – 8	5.393

Figure 4-4: Structure, composition and size of pure and iron doped cerium oxide particles.

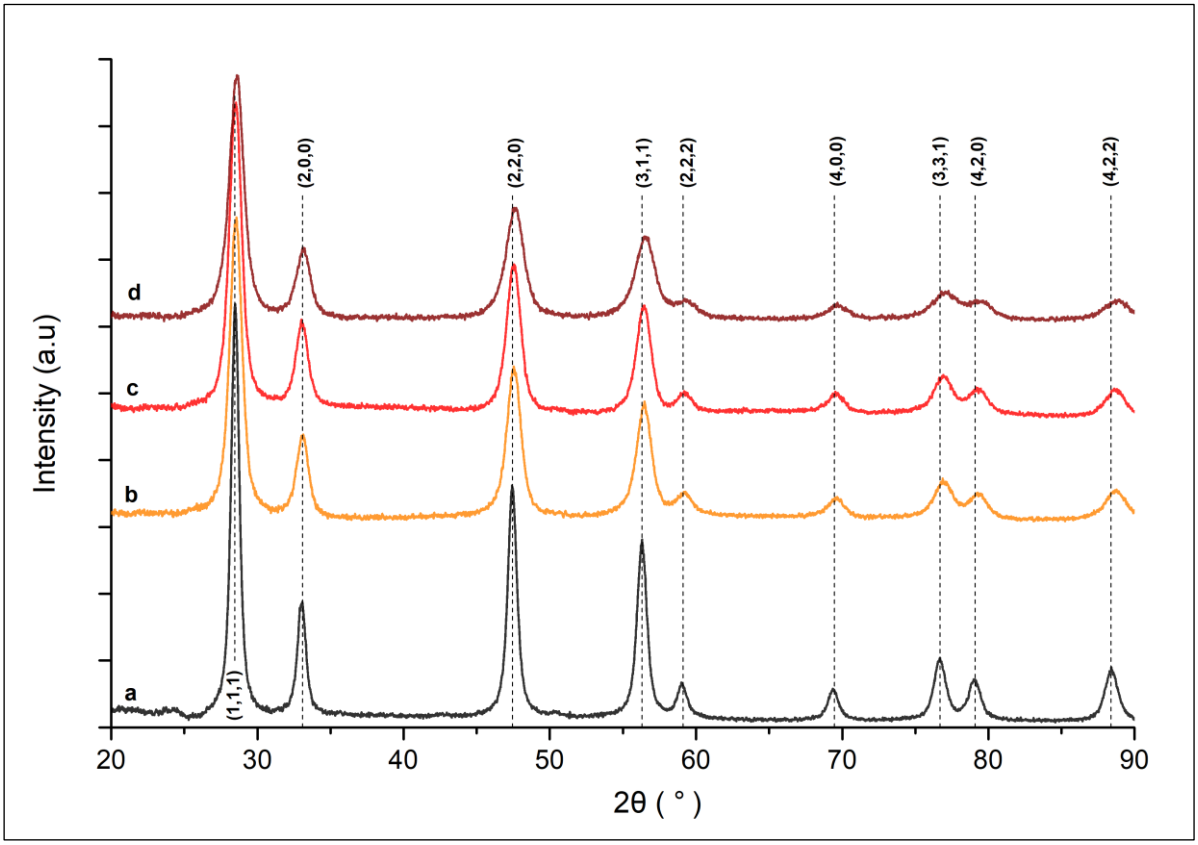

Figure 4-5: XRD reflection patterns for pure (a), 5% Fe doped (b), 10% Fe doped (c) and 20% Fe doped (d) cerium oxide particles synthesised by co-precipitate and annealed at 550 °C.

Some general trends in size and structure were:

- all crystals were of cubic-fluorite arrangement.
- crystal size increased with annealing temperature for each compositional variant
- the lattice parameter, a, reduced with increased crystal size.
- increasing the atomic concentration of iron reduced the lattice parameter, a

As expected, increasing the heat flow to precursor material increased the growth of the individual crystal while the lattice parameter shortened with crystallite size. The lattice parameter shortening is attributed to a decreasing population of Ce^{3+} ions in a crystal and is further investigated in section 4.1.4. For iron doped cerium oxide particles, the absence of detectable haematite (α-Fe_2O_3) or maghemite (γ-Fe_2O_3) peaks in all XRD patterns suggests that most included iron is substitutionally included. It's possible the 20% iron doped particles are covered with small amounts of interstitial iron oxide as a result of surpassing the solubility limit of the cerium oxide crystal [53]. The introduction of Fe^{3+} ions within the cerium oxide crystal lattice should have reduced the distance*, *d* between adjacent lattice planes and consequently the cell parameter, as the ionic radius of Fe^{3+} is 0.78Å compared to 0.97Å for Ce^{4+} ions and 1.14Å for Ce^{3+} ions [54]. Bragg's law dictates a reduction in *d* will result in an increased to the scatter angle, θ.

Equation 4-4 $$\boldsymbol{n/\lambda = 2dsin\theta \quad n = 1}$$

Analysis of Figure 4-5 confirms this shift of reflection peaks; being most prominent at the large angle reflection planes of 4,2,0 and 4,2,2. As expected the shift is greatest for the most heavily doped cerium oxide particles. The reduction of the lattice parameter, *a,* was confirmed through Rietveld refinement on individual XRD spectra.

In the case of the 550 ^{o}C annealing set the lattice parameter for the pure particle was found to be 5.416 Å with increasing iron doping reducing it to a minimum of 5.393 Å. It should be noted that the lattice parameter for bulk cerium oxide crystal is 5.410Å. The reduction in the d-space could potentially reduce crystal strain and subsequently reduce dynamic oxygen vacancies; increasing the lattice parameter. Alternatively, the opposite could be true; Fe^{3+} ions inhibit cerium oxide crystal growth and increase oxygen vacancies.

All that can be said at this stage is the lattice parameter is being affected by the inclusion of iron and any increase in oxygen vacancies due to diminished particle size is being masked by reduction in d-spacing within the cerium oxide crystal lattice.

EDS analysis of the composition of the cerium oxide particles determined sodium contamination at approximately 5 % atomic concentration. (Table 4-1) While sodium is essential component for mammalian metabolism [55] it's inclusion in this case could alter cell behaviour and affect the surface chemistry of the cerium oxide particles. As well the sodium displacement of cerium and iron affected the target atomic composition. Finally, the size of the 550^{o}C annealing set was large at ~14 nm meaning the radioprotection efficacy of the particles could not be assured. It was decided to synthesis the nanoparticles by flame spray pyrolysis instead.

*** The notation $d_{l,m,n}$ is used to denote the distance between adjacent lattice planes with the integers l, m, n being directional orthogonal parameters used to describe the plane in the x, y and z direction.**

4.1.4 Oxygen Vacancies Defects (OVD)

The need to produce three annealing sets of particles provided the opportunity to investigate the lattice parameter dependency on particle size for the pure cerium oxide particles. Past studies had shown an exponential increase in the lattice parameter as particles became small (3-10 nm) [21]. This rapid increase was explained by an increasing population of Ce^{3+} ions. As particles become small increased lattice strain affects oxygen vacancy defects nearby the surface of the crystal [58]. While the absolute value of the lattice parameter *a* as a function of the particle size did not agree with all literature the trend throughout was similar. This finding substantiates the idea that the lattice parameter of iron doped cerium oxide particles is representative of two phenomena; the inclusion of Fe^{3+} ions and the production of Ce^{3+} ions.

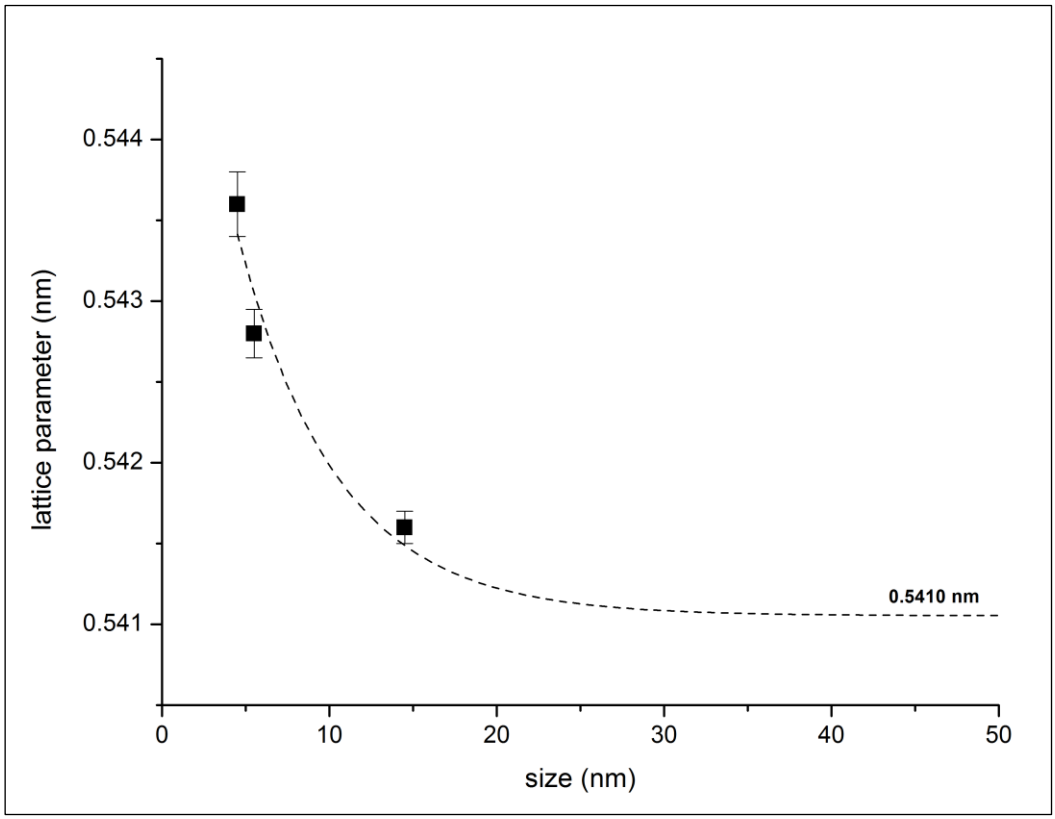

Figure 4-6: Oxygen vacancy defects increase with reduced crystal size.

4.2 Cerium oxide particles by spray pyrolysis

4.2.1 Synthesis

Figure 4-7: Cerium oxide particles formed by spray pyrolysis at 700 °C

Spray pyrolysis proved to be a less efficient method of synthesis than co-precipitation with an average yield of 60 % compared to 90 % for co-precipitation. What the synthesis process lacked in yield it made up for in sheer output as 80 g of finished product was produced in less than two days. More importantly the synthesis was able to produce small crystalline particles at far greater output than co-precipitation without a need for any further annealing. The particles were extremely dry and had a talc-like quality. Scanning electron microscope (SEM) analysis performed by a colleague showed the particles to be hollow spherical particles of 2-5 µm in diameter. During XRD studies pure cerium oxide particles were found to be very hygroscopic with the trait reducing as iron doping increased. The hygroscopic nature of cerium oxide particles is most probably due to uptake of water molecules in oxygen vacancies at the surface of the constituent crystals.

A reduction in hygroscopicity with the inclusion of Fe^{3+} iron suggests a reduction in these OVDs. While it is expected that Fe^{3+} ions will force oxygen vacancies in the lattice the uptake of oxygen species will be limited by the 4+ valence state of the neighbouring cerium ions.

4.2.2 Characterisation

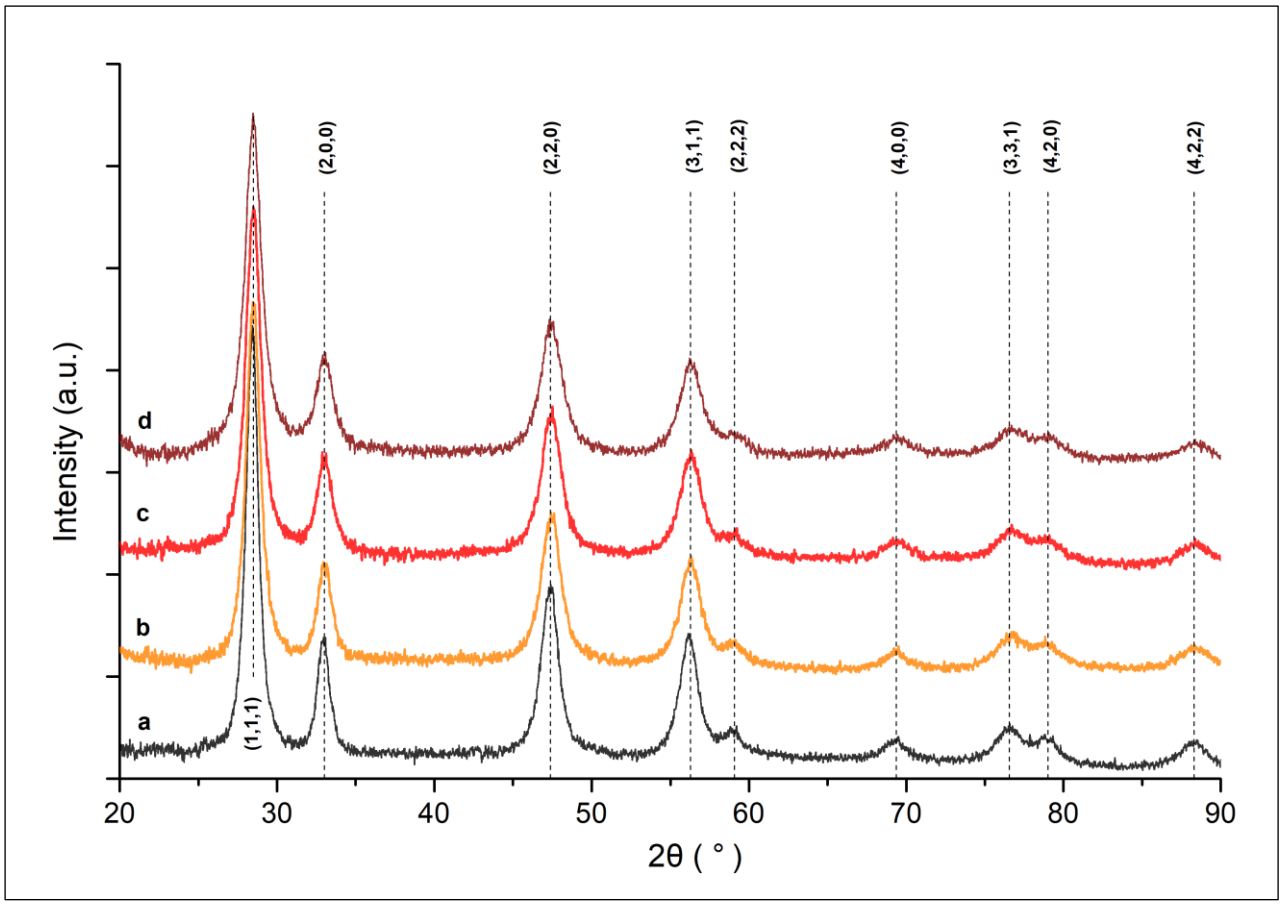

Figure 4-8: XRD reflection patterns for pure (a), 5% Fe doped (b), 10% Fe doped (c) and 20% Fe doped (d) cerium oxide particles synthesised by spray pyrolysis.

Studies of the x-ray diffraction patterns shown in Figure 4-8 report all particles to be of a single cubic-fluorite phase. The pattern was identified as cerium oxide and no evidence of haematite or maghemite crystals could be found. The broad peaks are consistent with small constituent crystallites.

As was the case with co-precipitation particles the following generalities could be found and are captured in Table 4-1:

- all crystals were of cubic-fluorite arrangement.
- the lattice parameter, a, reduced with increased crystal size.
- increasing the atomic concentration of iron reduced the lattice parameter, a

Of interest though was the size of crystals and the magnitude of the lattice parameter. Even though crystallisation occurred at 700 °C crystals were small (< 10 nm) and the lattice parameter for all particles well above bulk suggesting the formation of significant amounts of OVDs. This finding confirmed spray pyrolysis to be a superior synthesis method for the production of nanocrystalline cerium oxide particles. Furthermore, the doping outcome of the synthesis was excellent with actual atomic doping within 0.5 % of target for all particles except the 20 % iron doped variant. The loss of over 1 % atomic iron coupled with the plateauing of the lattice parameter at 5.416 Å suggests the solubility of iron within the cerium oxide crystal had been reached. Previously a solubility limit of between 10-20 % had been reported by Truffault et al. [59]. At such high crystallisation temperatures it's highly likely that the iron was evaporated at the head of the head of the oven.

Particle	Atomic composition by ICP-OES		Anneal (°C)	Crystallite size (nm)	*a* (Å)
	Ce (%)	Fe (%)			
Pure	99.8 ± 0.3	0.23 ± 0.01	700	7 - 10	5.428
5% Fe	95.3 ± 0.4	4.74 ± 0.02	700	6 - 9	5.419
10% Fe	90.4 ± 0.3	9.57 ± 0.04	700	5 - 8	5.416
20% Fe	81.1 ± 0.5	18.91 ± 0.01	700	5 - 7	5.416

Table 4-1: Synthesis and structure of spray pyrolysis cerium oxide particle

As seen previously Fe^{3+} ion inclusion reduces crystallite size most likely due to its reduced co-ordinate geometry and the distortion of the lattice as a result of its smaller ionic radius. Again, the lattice parameter *a* for each particle must be consider to be a net outcome from the inclusion of Fe^{3+} ions and the generation of Ce^{3+} ions as a result strain within crystals.

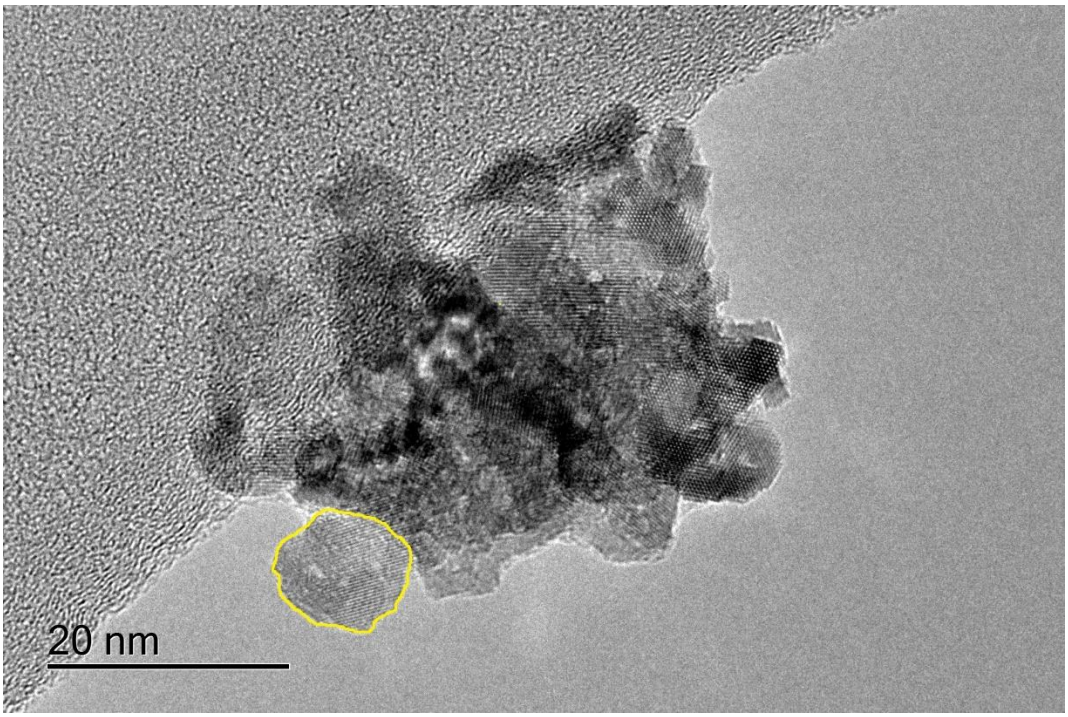

Figure 4-9: TEM image of pure cerium oxide nanoparticle (~ 40 nm) made up of small crystals (~ 10 nm). The highlighted yellow is 2 crystals co-joined. The smaller crystal approximated at 8 nm.

The initial goal of TEM was to verify crystallite size and lattice parameter. However, it became quickly apparent that the sintered aggregation of crystals would be a roadblock to this objective. Compounding this was the blurring of images caused by earthworks in the adjacent block to ISEM. This affected all iron doped nanoparticles as images were taken on a separate day to the pure cerium oxide nanoparticles. There were enough useful images to confirm the effectiveness of the new sonication method with particles as small as 30-50 nm seen, but not imaged for all particles; pure and iron doped. In Figure 4-9 is a pure cerium oxide nanoparticle of ~ 40 nm diameter made up of small crystals of ~ 10 nm dimension. The highlighted yellow is 2 crystals co-joined.

The smaller crystal approximated at 8 nm. The small amount of exposed crystals imaged, like that outlined yellow above had dimensions consistent with those determined by XRD. Due to the disinclination of the fused boundaries determination of lattice parameters was not possible.

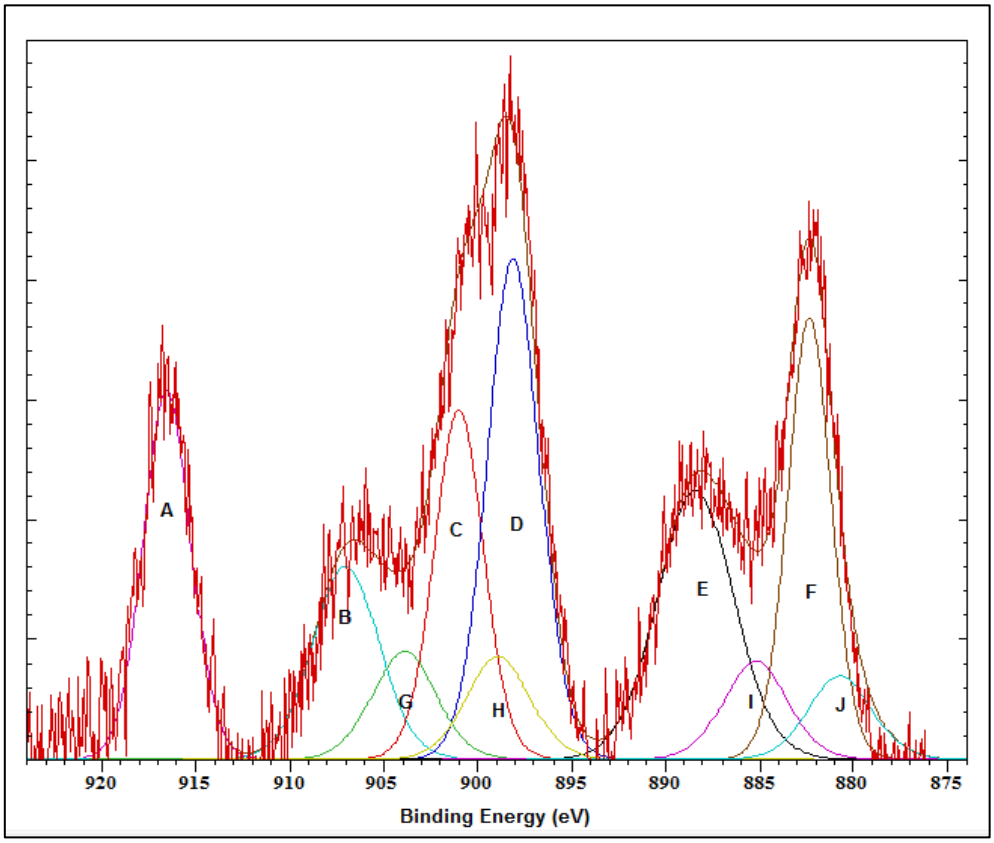

Figure 4-10: XPS spectra for Ce 3d binding energy peaks – pure cerium oxide nanoparticles.

The bulk cerium oxide spectra possesses 6 orbital peaks due to d-splitting caused by the interaction of the oxygen 2p valence band with the Ce 4f electron band [60]. This makes it extremely difficult to identify the spin-orbital components peaks of the Ce^{3+} ion. Figure 4-10 shows the Ce3d spectra to be very crowded with the Ce^{4+} triplet for the $3d_{5/2}$ energy state (D, E, F) overlapping the Ce^{4+} triplet for the $3d_{3/2}$ energy state (A,B,C) with the Ce^{3+} doublet for the $3d_{5/2}$ energy state (I,J) and the Ce^{3+} doublet for the $3d_{3/2}$ energy state (G,H) to be found amongst them.

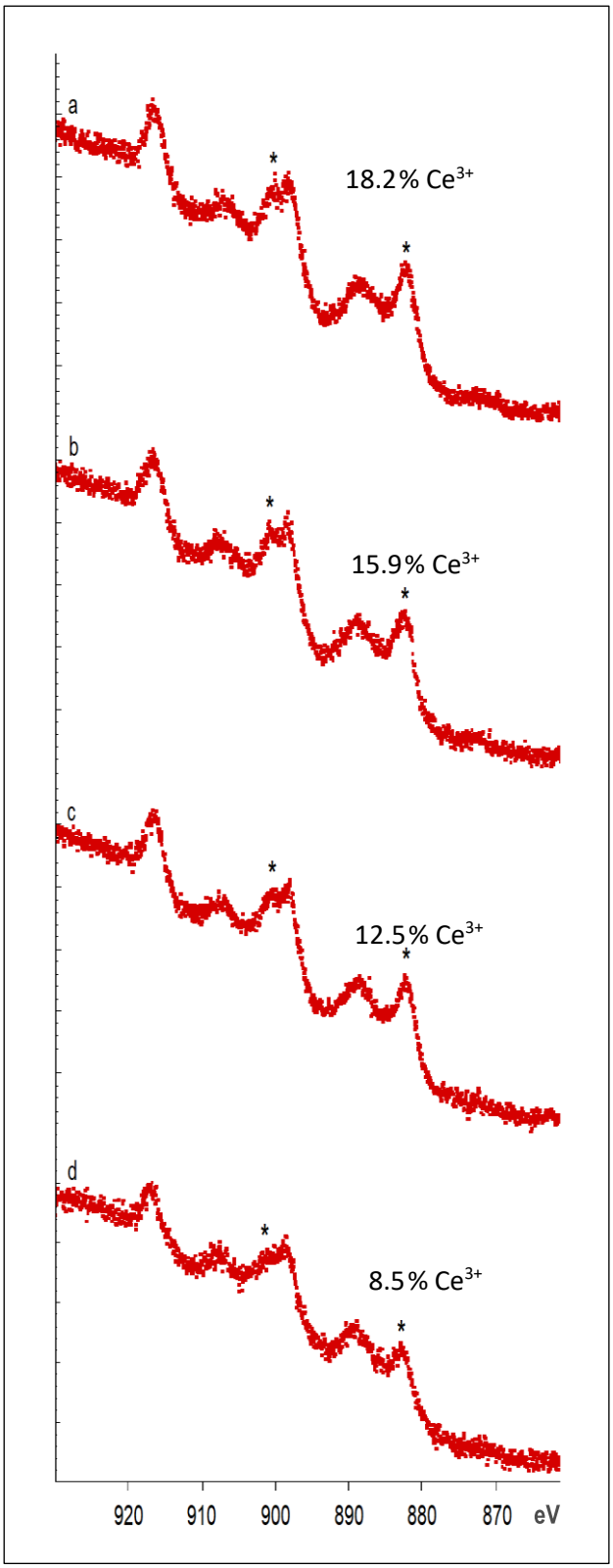

Figure 4-11: Ce 3d XPS spectra of pure (a), 5 % Fe (b), 10 % Fe (c) and 20 % Fe doped nanocrystalline particles.

To determine Ce ion portions the background was removed using Shirley subtraction and spin-orbit components peaks built as described in Table 3-3. The results were as expected with pure CeOx NPs possessing the largest atomic population of Ce^{3+} ions at 18.2% with populations trending to a minimum of 8.5% for the 20 % iron doped cerium oxide particle. A greater comparative analysis of the Ce3d survey spectra for all CeOx NP (Figure 4-11) identify diminishing peaks at 900.8 and 882.3 eV. The diminishing peaks are within 2-3 eV of peaks G and I suggesting the involve of the Ce^{3+} doublets and a reducing population of Ce^{3+} ions with increased Fe^{3+} ions.

4.2.3 Cell growth

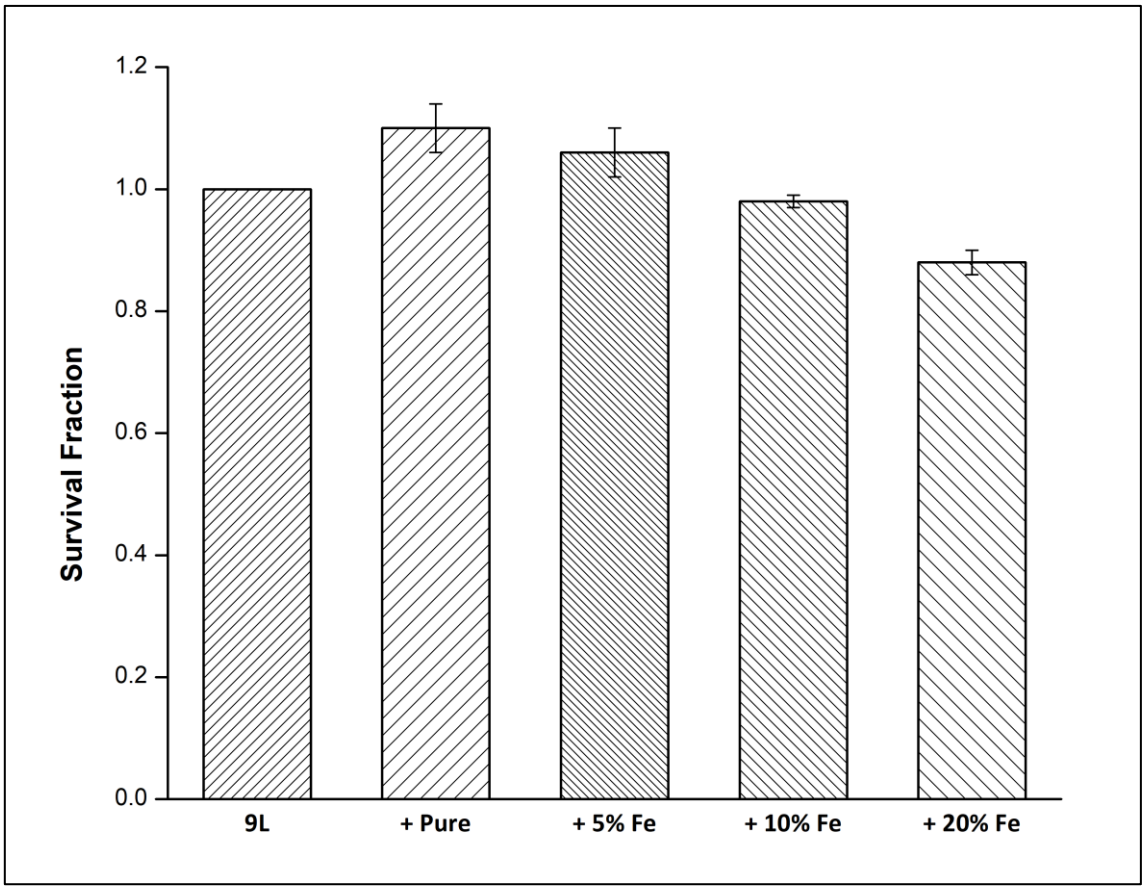

Figure 4-12: 9L cell growth with cerium oxide nanoparticle inclusions. Survival fractions were normalised to a 9L control, averages determined from a sample size of 2 and errors given as ± 1 standard deviation from the mean.

It was found that pure and 5% iron doped cerium oxide nanoparticles boosted cell growth while 10% iron doped cerium oxide nanoparticles had no statistically significant effect. The survival fraction for each nanoparticle inclusion was 1.10±0.04 (1SD), 1.06±0.04 (1SD) and 0.98±0.01 (1 SD) respectively.

It should be noted that the survival fractions of pure and 5% Fe doped CeOx NP inclusions were not statistically significant. However, the trend of diminishing cell growth in figure 4-12 is significant and consistent with modulated antioxidant capacity. Increasing iron levels reduces lattice strain and the number of oxygen vacancies forming in the crystal. The trend supports early work demonstrating a direct correlation between the trivalent oxidation state of CeOx NPs and superoxide-dismutase mimetic-activity [61]. The 20% iron doped cerium oxide nanoparticle possessed mild toxicity reducing the survival fraction to 0.88±0.02 (1SD). This result was not unexpected as characterisation of the NP suggested a small amount of interstitial hematite or maghemite forming throughout the NP. Previous investigation by Cardillo had shown maghemite to be quite toxic to the 9L cell line [62].

4.2.4 Radiation Protection

Due to a sudden and sustained deterioration of 9L cell line health towards the end of investigations it was only possible to produce survival curves for the 9L control and the pure CeOx NP inclusion (Figure 4-13). A complete study of radioprotection for all nanoparticle inclusions was achieved instead by comparing survival fractions at a single dose of 8Gy (Figure 4-14).

The protection afforded by the pure CeOx NP inclusion is evident by the increased shoulder of the *9L + pure NP* curve compared to the *9L control* curve. This increased shoulder suggests an increased portion of cells sustained sub lethal damage at lower doses (< 5 Gy) and were able to repair over the 3 weeks of incubation.

A linear- quadratic fit of the curves reports α/β ratios of 6.32 for the *9L control* versus 2.80 for the *9L+pure CeOx NPs*. The increased radioresistance of this cell line series was confirmed with a PER of 1.22. At 10% survival fraction the 9L control line could sustained 8.39 Gy while the NP inclusion a larger 10.22 Gy. This finding is similar to that reported by Briggs, 2013 [48]. Brigg's PER of 1.26 was achieved will slightly smaller cerium oxide nanoparticles possessing slightly smaller crystals of 4-7 nm. The smaller size of these crystals should improve free radical scavenging [63]. However, the particles were annealed at a much lower temperature of 500 °C. It's possible that nitrates left behind during synthesis gave these nanoparticles a slight cytotoxicity which countered the positive scavenging effect [64] resulting in a reduced overall improvement.

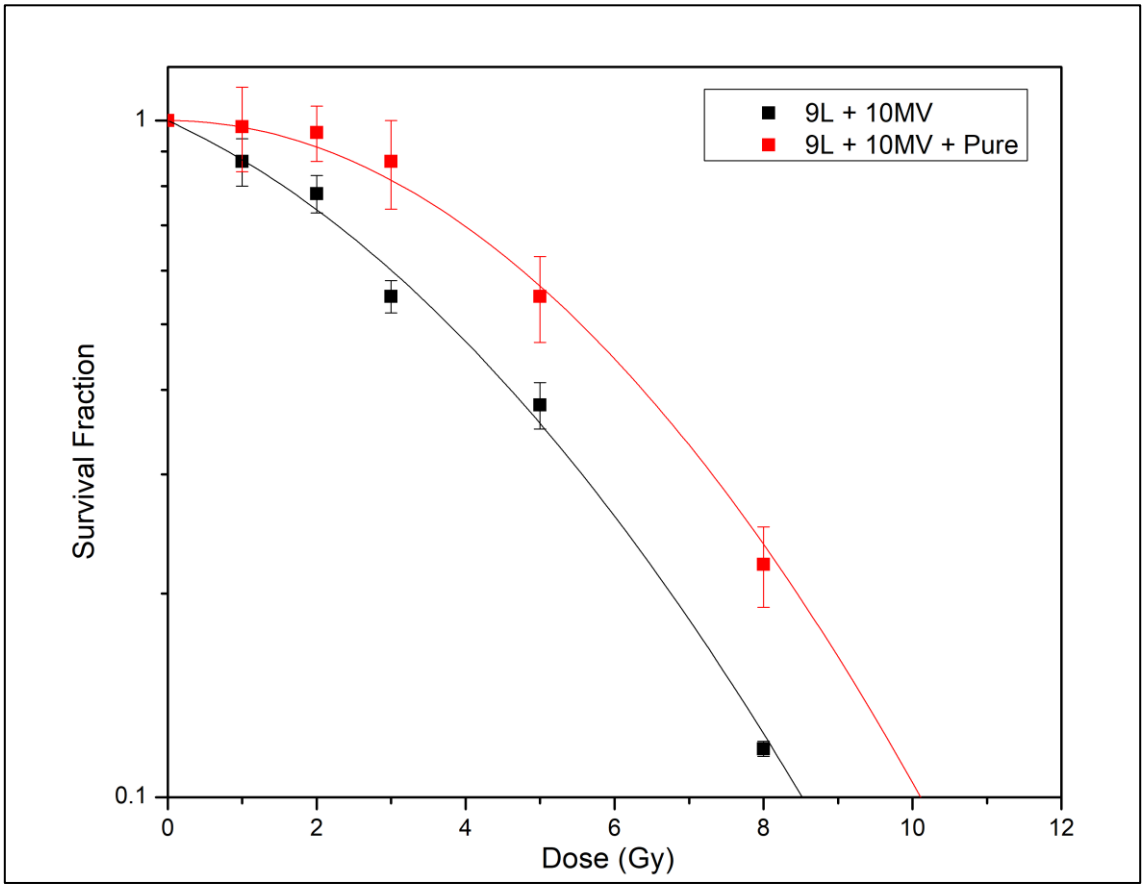

Figure 4-13: Survival curves of 9L control and CeOx NP inclusion for 10MV x-rays. Survival fractions were normalised to 9L control, averages determined from a sample size of 2 and errors given as ± 1 standard deviation from the mean.

The radioresistance of the 9L cell line is attributed to the proliferation of cells themselves. The large number of cells lower the pH of the media through the contribution of metabolic waste compounds such as lactic acid and carbon dioxide which in turn reduce the amount of dissolved oxygen in the media [65]. This acidic shift is seen as a change in the media colour from purple to orange (pH=8.5 → pH=7.5). The reduced oxygen levels should result in the formation of fewer reactive oxygen species during the megavoltage irradiation [66].

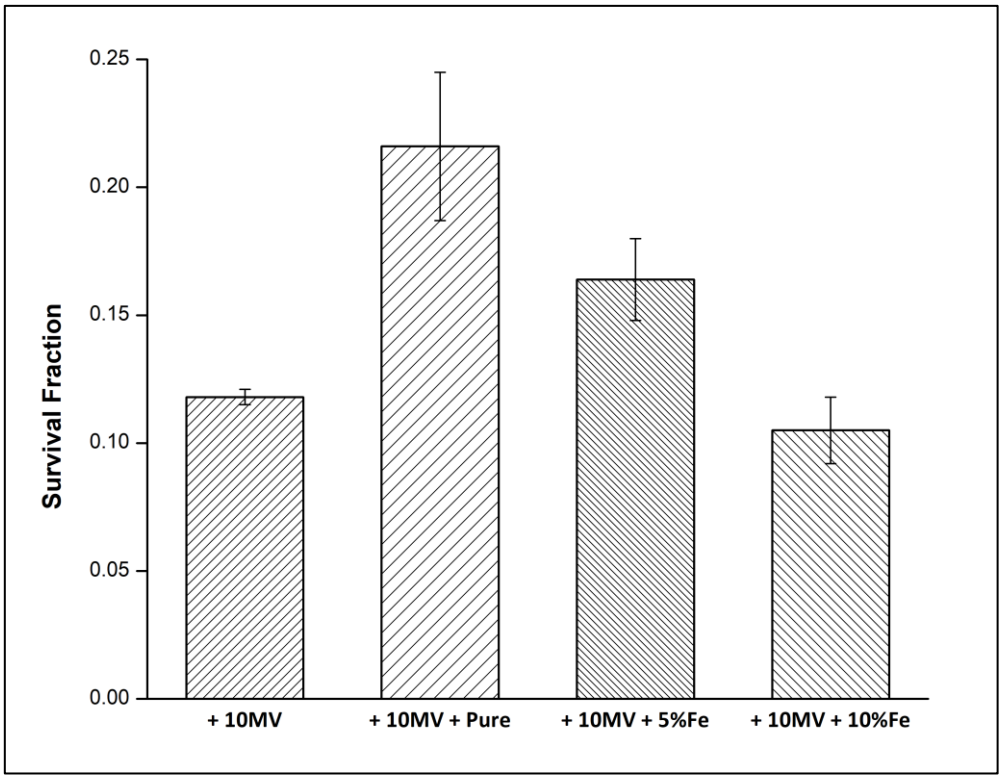

Figure 4-14: Surviving fraction of 9L cells for cerium oxide nanoparticles after delivery of 8 Gy absorbed dose. SF were normalised to 9L control, averages determined from a sample size of 2 and errors given as ± 1 standard deviation from the mean.

Assessing survival curves (Figure 4-13) 8Gy was chosen as the most suitable absorbed dose for investigation of radioprotection across all three NP inclusions. Firstly, the difference in survival fraction between the *9L control* curve and *9L + pure NP* curve provided a good range for further investigation.

Secondly, the absorbed dose was clinically relevant. The use of SABR for local tumour control in sites such as lung has seen a large increase in hypo-fractionated therapies [67].

The survival fractions for 9L control and 9L with pure, 5 % and 10 % iron doped CeOx NP inclusions were 0.118 ± 0.003 (1SD), 0.21 ± 0.03 (1SD), 0.16 ± 0.02 (1SD) and 0.11 ± 0.1 (1SD) respectively. As expected, the pure cerium oxide nanoparticle showed a good improvement in survival fraction; doubling that of the control. The 5 % iron doped cerium oxide NP also increased the survival fraction by 6%, less so than the pure CeOx NP. The 10 % iron doped CeOx NP showed no protection.

In review it can be seen that radiation protection correlates well with nanoparticle cell growth impact. These results are consistent with the hypothesis that radiation protection is dependent on the population of Ce^{3+} ion population in the nanoparticle.

Chapter 5

Conclusion

The goal of this thesis centred on the anti-oxidant capacity of cerium oxide nanoparticles (CeOx NPs), and specifically, to investigate whether this antioxidant dependence translated to radiation protection efficacy. The hypothesis of this thesis was that cerium oxide nanoparticles doped with iron (Fe^{3+}) to 5%, 10% and 20% atomic concentrations would demonstrate dependence of radiation protection efficacy by varying the population of Ce^{3+} atoms within each particle.

5.1 Synthesis and characterisation

The production of pure and iron doped cerium oxide particles by spray pyrolysis was shown to be far superior to that of co-precipitation owing to the high output rate, accurate doping, high crystallinity and the small size of the constituent crystals making up the CeOx particles (5 – 10 nm). 80 g of extremely dry particle powder was produced in 2 days with all powders exhibiting talc-like consistency; a potential indication of porous structure.

The porosity of one particle was confirmed by D. Cardillo (09.03.2016) when performing a parallel study with BET analysis on the 5% iron doped CeOx particles determining a specific surface area of ~47 m^2/g. It should be remembered this particle will later be sonicated to a volume some 10^6 times smaller than synthesised, increasing this value immensely. ICP-OES analysis of chemical composition reported minimal contamination and achievement of target doping concentrations to within 0.5 % (absolute) for all but the 20% iron doped CeOx particles. The consensus was the 20% atomic concentration target was above the solubility limit of cerium oxide as reported in the literature [53].

Later toxicity studies supported this view as the nanoparticle exhibited mild toxicity on 9L and MDCK cell lines; reducing survival fraction respectively to 0.88 ± 0.02 and 0.90 ± 0.03. Through XRD analysis all particles were shown to be of a single cubic fluorite phase with a reflection pattern identified as that of cerium oxide. The average crystallite size range of 6 - 8 nm in a single dimension was deemed acceptable for controlling the population of Ce^{3+} ions in lattice. TEM imaging of CeOx particles confirmed crystallite sizes of 8 ± 1 nm, 7 ± 1 nm, 6 ± 1 nm and 6 ± 1 nm for pure and 5%, 10% and 20% CeOx particles respectively.

Due to a lack of experience in the technology TEM was underutilised resulting in limited structural information about all particles. In hindsight, lower magnification SEM images focussing on the size and shape of individual crystals and their greater co-ordination within the aggregate would have been more informative. A reducing lattice parameter with increased iron doping confirmed the inclusion of the Fe^{3+} ions within the cerium oxide lattice. Rietveld refinement determine the minimum lattice parameter to be 5.416 Å; suggesting the production of Ce^{3+} ion within lattice for all particles.

Investigation of the particles using XPS showed a decreasing population of Ce^{3+} ions with increasing iron doping; from 18.2 % in pure cerium oxide nanoparticles to 8.2 % for the 20 % iron doped variant. This trend suggests the inclusion of Fe^{3+} ions are affecting the population of Ce^{3+}; possibly by reducing strain in the crystal lattice and subsequently the number of oxygen vacancy defects. Curve fitting component peaks to the Ce3d spectra proved challenging. There was a total of 10 residing peaks with 5 of those peaks occupying only 15 eV. In Figure 4-11 the diminishing peaks of the survey spectra at 900.8 and 882.3 eV confirm a reduction in Ce^{3+} ion population.

If it were a reduction in Ce^{4+} ion population it can be reasoned all triplet intensities ($3d_{5/2}$ and $5d_{3/2}$) would diminish due to the electronic correlation effect - quantum interplay.

Reviewing the distribution of all spin-orbit peaks in the 3d spectra (Figure 4-10) and past literature it's the view of the author that a better fit would be achieved if peaks G and I were 3-5 eV lower in BE. The possible outcome of this shift would see an increased portion of Ce^{3+} ions within all particles. Unfortunately, at the time of writing, access to XPS analysis software was not possible. Regardless of this, the fit of peaks for all particle spectra clearly implies a reduced Ce^{3+} ion population was achieved with increased Fe^{3+} doping. Further studies on the Ce3d spectra to arrive at a more accurate quantification of cerium 3+ ion concentrations will be conducted in the near future.

5.2 Biological assessment

Clonogenic assays using 9L gliosarcoma cells assessed cell growth impact and radiation protection efficacy. Pure cerium oxide nanoparticles provided a 10% boost to cell growth. When irradiated with 10 MV x-rays this boost translated to a performance enhancement ratio of 1.22. At 8 Gy the pure CeOx NP inclusion improved the radiation survival fraction by 75%, from 0.12 to 0.22. 5% Fe doped CeOx NPs improved cell growth by 6% and increased the radiation survival fraction by 20% to 0.16. 10% Fe doped CeOx NPs did not significantly affect cell growth or radiation survival fraction. As stated previously 20% iron doped NPs were exhibited low/mild toxicity on account of possible haematite or maghemite impurities. Overall these studies suggest that radiation protection efficacy of cerium oxide nanoparticles is dependent on the population of Ce^{3+} ions within the crystal lattice and is consistent with previous findings.

5.3 Future studies

Glycolysis allows cancer cells to maintain homeostasis and survive under prolonged hypoxia [68]. Cancer cells have evolved to favour glycolytic metabolism over oxidative even when there is ample supply of oxygen [69]. The production of lactic acid through this metabolic pathway results in a comparatively lower local pH than normal tissue. The pH of normal tissue, being closer to neutral, is more favourable for free radical scavenging [41].

So why then is the 9L cell line, a cancer analog, selective for radioprotection? Most likely this is an artefact of the study. At 90% flask confluence the increased lactic output of the 9L cell monolayer shifts the basic media solution to neutrality. As cells are metabolic throughout radiation exposure and for some time after the pH of the media will remain unchanged till plating. The included cerium oxide NPs are actively scavenging throughout this time. The exact reason for this selectivity cannot be confirmed at present and the matter warrants future study.

5.4 Final Statement

Like all scientific endeavours the success of this investigation hinged on the ability to control multiple variables in an attempt to assess the effect of changing just one. In the world of radio-biology this is not an easy task and at some points in this investigation the best that could be done was to assess the global rather than the multitude of variations at the local. However, it is the view of the author that this gauge of assessment in no way undermines the integrity of the work completed for this study. In review and under scrutiny the evidence collected during this investigation supports the hypothesis:

The radio protection efficacy of cerium oxide nanoparticles is dependent upon the population of Ce^{3+} ion within the crystal lattice.

References

[1] Ivana Celardo, Milena De Nicola, Corrado Mandoli, Jens Z Pedersen, Enrico Traversa, and Lina Ghibelli, 'Ce3+Ions Determine Redox-Dependent Anti-apoptotic Effect of Cerium Oxide Nanoparticles', *Ce3Ions Determine Redox-Depend. Anti-Apoptotic Eff. Cerium Oxide Nanoparticles*, vol. 5, no. 6, pp. 4537–4549, 2011.

[2] M. Beyzadeoglu, G. Ozyigit, and C. Ebruli, 'Radiobiology', in *Basic Radiation Oncology*, Berlin Heidelberg: Springer Verlag, 2010, pp. 71–142.

[3] Australian Institute of Health and Welfare, 'Cancer in Australia 2017', 101, 2017.

[4] R. Warters, K. Hofer, and J. Smith, 'Radionuclide toxicity in cultured mammalian cells: elucidation of the primary site of radiation damage.', *Curr Top Radiat Res*, vol. 12, pp. 389–407, 1997.

[5] E. Hall and A. Giaccia, *Radiobiology for the Radiologist*, 7th ed. Philadelphia, USA: Lippincott, Williams and Wilkins, 2012.

[6] D. Goodhead and H. Nikijoo, 'Track structure analysis illustrating the prominent role of low-energy electrons in radiobiological effects of low-LET radiations.', *Phys Med Biol*, vol. 36, pp. 229–238, 1991.

[7] P. Bryant, *Mechanism of repair of DNA damage induced by ionizing radiation. The Biological Basis of Radiotherapy.*, Second. Amsterdam: Elsevier Publishers, 1989.

[8] M. Knowles and P. Selby, *Intoduction to the Cellular and Molecular Biology of Cancer*. Oxford: Oxford Bioscience, 2005.

[9] J. Bushberg *et al.*, *The Essential Physics of Medical Imaging*, 3rd Ed. Philadelphia, USA: Lippincott, Williams and Wilkins, 2002.

[10] D. Thames and J. Hendry, *Fractionation in radiotherapy*. New York: Taylor and Francis, 1987.

[11] ICRP, ‘The 2007 Recommendations of the International Commission on Radiological Protection.’, *ICRP Publ. 103*, vol. Ann. ICRP 37, no. 2–4, 2007.

[12] M. Doran and I. Dayman, ‘Australian-first cancer facility flagged for Adelaide’, 2017. [Online]. Available: http://www.abc.net.au/news/story-streams/federal-budget-2017/2017-05-06/federal-budget-2017-cancer-facility-flagged-for-adelaide/8502564. [Accessed: 08-Sep-2017].

[13] B. Barton, S. Jacob, K. Wong, S. Thomson, T. Hanna, G. Delaney, *et al.*, ‘Estimating the demand for radiotherapy from the evidence: a review of changes from 2003 to 2012.’, *Radiother. Oncol.*, vol. 112, no. 1, pp. 140–144, 2014.

[14] F.R.O., ‘Position Paper Techniques and Technologies in Radiation Oncology 2015 Horizon Scan Australia and New Zealand’, *RANZCR*, 2016.

[15] P. Metcalfe, T. Kron, and P. Hoban, *The Physics of Radiotherapy X-rays and Electrons*. Madison, Wisconsin: Medical Physics Publishing, 2007.

[16] K. J. Ray, N. R. Sibson, and A. E. Kiltie, ‘Treatment of Breast and Prostate Cancer by Hypofractionated Radiotherapy: Potential Risks and Benefits’, *Clin. Oncol.*, vol. 27, no. 7, pp. 420–426, Jul. 2015.

[17] T. Hellevik and I. Martinez-Zubiaurre, ‘Radiotherapy and the Tumor Stroma: The Importance of Dose and Fractionation’, *Front. Oncol.*, vol. 4, 2014.

[18] C. Goldsmith and A. Gaya, ‘Stereotactic ablative body radiotherapy (SABR) for primary and secondary lung tumours’, *Cancer Imaging*, vol. 12, no. 2, pp. 351–360, 2012.

[19] R. Kohen and A. Nyska, ‘Invited Review: Oxidation of Biological Systems: Oxidative Stress Phenomena, Antioxidants, Redox Reactions, and Methods for Their Quantification’, *Toxicol. Pathol.*, vol. 30, no. 6, pp. 620–650, Oct. 2002.

[20] D. Citrin, A. P. Cotrim, F. Hyodo, B. J. Baum, M. C. Krishna, and J. B. Mitchell, ‘Radioprotectors and Mitigators of Radiation-Induced Normal Tissue Injury’, *The Oncologist*, vol. 15, no. 4, pp. 360–371, Apr. 2010.

[21] S. Xavier *et al.*, 'Differential protection by nitroxides and hydroxylamines to radiation-induced and metal ion-catalyzed oxidative damage', *Biochim. Biophys. Acta BBA - Gen. Subj.*, vol. 1573, no. 2, pp. 109–120, Nov. 2002.

[22] J. R. Kouvaris, V. E. Kouloulias, and L. J. Vlahos, 'Amifostine: The First Selective-Target and Broad-Spectrum Radioprotector', *The Oncologist*, vol. 12, no. 6, pp. 738–747, Jun. 2007.

[23] B. P. Soule *et al.*, 'Therapeutic and Clinical Applications of Nitroxide Compounds', *Antioxid. Redox Signal.*, vol. 9, no. 10, pp. 1731–1744, Oct. 2007.

[24] I. Takahashi, T. Nagai, K. Miyaishi, Y. Maehara, and H. Niibe, 'Clinical study of the radioprotective effects of amifostine (YM-08310, WR-2721) on chronic radiation injury', *Int. J. Radiat. Oncol.*, vol. 12, no. 6, pp. 935–938, Jun. 1986.

[25] J. Gu, S. Zhu, X. Li, H. Wu, Y. Li, and F. Hua, 'Effect of Amifostine in Head and Neck Cancer Patients Treated with Radiotherapy: A Systematic Review and Meta-Analysis Based on Randomized Controlled Trials', *PLoS ONE*, vol. 9, no. 5, p. e95968, May 2014.

[26] K. Ranganathan, E. Simon, J. Lynn, *et al.*, 'Novel Formulation Strategy to Improve the Feasibility of Amifostine Administration', *Pharm Res*, vol. 35, no. 99, 2018.

[27] P. Jasinski, T. Suzuki, and H. U. Anderson, 'Nanocrystalline undoped ceria oxygen sensor', *Sel. Pap. Eurosensors XVI*, vol. 95, no. 1, pp. 73–77, Oct. 2003.

[28] R. J. Farrauto and R. M. Heck, 'Catalytic converters: state of the art and perspectives', *Catal. Today*, vol. 51, no. 3, pp. 351–360, Jul. 1999.

[29] J. Kašpar, P. Fornasiero, and N. Hickey, 'Automotive catalytic converters: current status and some perspectives', *Fundam. Catal. Appl. Environ. Probl.*, vol. 77, no. 4, pp. 419–449, Jan. 2003.

[30] C. L. Campos, C. Roldán, M. Aponte, Y. Ishikawa, and C. R. Cabrera, 'Preparation and methanol oxidation catalysis of Pt-CeO2 electrode', *J. Electroanal. Chem.*, vol. 581, no. 2, pp. 206–215, Aug. 2005.

[31] Lily L. Wong, Suzanne M. Hirst, Quentin N. Pye, Christopher M. Reilly, Sudipta Seal, and James F. McGinnis, 'Catalytic Nanoceria Are Preferentially Retained in the Rat Retina and Are Not Cytotoxic after Intravitreal Injection', *Catal. Nanoceria Are Prefer. Retain. Rat Retina Are Cytotoxic Intravitreal Inject.*, vol. 8, no. 3, 2013.

[32] Atul Asati, Santimukul Santra, Charalambos Kaittanis, Sudip Nath, and J. Manuel Perez, 'Oxidase-Like Activity of Polymer-Coated Cerium Oxide Nanoparticles', *Oxidase-Like Act. Polym. Cerium Oxide Nanoparticles*, vol. 48, no. 13, pp. 2308–2312, 2009.

[33] Karin L Heckman *et al.*, 'Custom Cerium Oxide Nanoparticles Protect against a Free Radical Mediated Autoimmune Degenerative Disease in the Brain', *Cust. Cerium Oxide Nanoparticles Prot. Free Radic. Mediat. Autoimmune Degener. Dis. Brain*, vol. 7, no. 12, pp. 10582–10596, 2013.

[34] Roy W Tarnuzzer, Jimmie Colon, Swanand Patil, and Sudipta Seal, 'Vacancy Engineered Ceria Nanostructures for Protection from Radiation-Induced Cellular Damage', *Vacancy Eng. Ceria Nanostructures Prot. Radiat.-Induc. Cell. Damage*, vol. 5, no. 12, pp. 2573–2577, 2005.

[35] P-T. Xu *et al.*, 'Cerium Oxide Nanoparticles: A Potential Medical Countermeasure to Mitigate Radiation-Induced Lung Injury in CBA/J Mice', *Cerium Oxide Nanoparticles Potential Med. Countermeas. Mitigate Radiat.-Induc. Lung Inj. CBAJ Mice*, vol. 185, no. 5, pp. 516–526, 2016.

[36] Sameer Deshpande, Swanand Patil, Satyanarayana VNT Kuchibhatla, and Sudipta Seal, 'Size dependency variation in lattice parameter and valency states in nanocrystalline cerium oxide', *Size Depend. Var. Lattice Parameter Val. States Nanocrystalline Cerium Oxide*, vol. 87, no. 13, p. 133113, 2005.

[37] A. Macedo, S. E. Fernandes, A. Valente, R. A. Ferreira, L. Carlos, and J. Rocha, 'Catalytic Performance of Ceria Nanorods in Liquid-Phase Oxidations of Hydrocarbons with tert-Butyl Hydroperoxide', *Molecules*, vol. 15, no. 2, pp. 747–765, Feb. 2010.

[38] A. Souza de Araujo, J. Carlos Diniz, A. O. S. da Silva, and R. A. Alves de Melo, 'Hydrothermal synthesis of cerium aluminophosphate', *J. Alloys Compd.*, vol. 250, no. 1, pp. 532–535, Mar. 1997.

[39] Sian Masson, Peter Holliman, Maher Kalaji, and Petr Kluson, 'The production of nanoparticulate ceria using reverse micelle sol gel techniques', *Prod. Nanoparticulate Ceria Using Reverse Micelle Sol Gel Tech.*, vol. 19, no. 21, pp. 3517–3522, 2009.

[40] Neil J. Lawrence *et al.*, 'Defect Engineering in Cubic Cerium Oxide Nanostructures for Catalytic Oxidation', *Defect Eng. Cubic Cerium Oxide Nanostructures Catal. Oxid.*, vol. 11, no. 7, pp. 2666–2671, 2011.

[41] J. M. Perez, A. Asati, S. Nath, and C. Kaittanis, 'Synthesis of Biocompatible Dextran-Coated Nanoceria with pH-Dependent Antioxidant Properties', *Small*, vol. 4, no. 5, pp. 552–556, May 2008.

[42] Rafael A. Madero-Visbal *et al.*, 'Harnessing nanoparticles to improve toxicity after head and neck radiation', *Harnessing Nanoparticles Improve Toxic. Head Neck Radiat.*, vol. 8, no. 7, pp. 1223–1231, 2012.

[43] Jimmie Colon *et al.*, 'Cerium oxide nanoparticles protect gastrointestinal epithelium from radiation-induced damage by reduction of reactive oxygen species and upregulation of superoxide dismutase 2', *Cerium Oxide Nanoparticles Prot. Gastrointest. Epithelium Radiat.-Induc. Damage Reduct. React. Oxyg. Species Upregulation Superoxide Dismutase 2*, vol. 6, no. 5, pp. 698–705, 2010.

[44] Jimmie Colon *et al.*, 'Protection from radiation-induced pneumonitis using cerium oxide nanoparticles', *Prot. Radiat.-Induc. Pneumonitis Using Cerium Oxide Nanoparticles*, vol. 5, no. 2, pp. 225–231, 2009.

[45] Atul Asati, Santimukul Santra, Charalambos Kaittanis, and J Manuel Perez, 'Surface-Charge-Dependent Cell Localization and Cytotoxicity of Cerium Oxide Nanoparticles', *Surf.-Charge-Depend. Cell Localization Cytotox. Cerium Oxide Nanoparticles*, vol. 4, no. 9, pp. 5321–5331, 2010.

[46] Laurianne Truffault *et al.*, 'Application of nanostructured Ca doped CeO2 for ultraviolet filtration', *Appl. Nanostructured Ca Doped CeO2 Ultrav. Filtr.*, vol. 45, no. 5, pp. 527–535, 2010.

[47] A. Namukin, A. Kraut-Vass, W. Gaarenstroom, and C. Powell, 'NIST X-ray Photoelectron Spectroscopy Database', 2012. .

[48] Adam Briggs *et al.*, 'Cerium oxide nanoparticles: influence of the high-Z component revealed on radioresistant 9L cell survival under X-ray irradiation', *Cerium Oxide Nanoparticles Influ. High-Z Compon. Reveal. Radioresistant 9L Cell Surviv. X-Ray Irradiat.*, vol. 9, no. 7, pp. 1098–1105, 2013.

[49] Y. Grigoryev, 'Cell counting with a haemocytometer: Easy as 1,2,3.', 08-Dec-2014. .

[50] N. A. P. Franken, H. M. Rodermond, J. Stap, J. Haveman, and C. van Bree, 'Clonogenic assay of cells in vitro', *Nat. Protoc.*, vol. 1, no. 5, pp. 2315–2319, Dec. 2006.

[51] C. S. Bruning-Fann and J. B. Kaneene, 'The effects of nitrate, nitrite and N-nitroso compounds on human health: a review.', *Vet. Hum. Toxicol.*, vol. 35, no. 6, pp. 521–538, Dec. 1993.

[52] R. K. Hailstone, A. G. DiFrancesco, T. D. Allston, K. Parsiegla, and K. J. Reed, 'Is iron doping of nanoceria possible at low temperature?', *Iron Doping Nanoceria Possible Low Temp.*, vol. 16, no. 3, 2014.

[53] Laurianne Truffault *et al.*, 'Synthesis and Characterization of Fe Doped CeO2 Nanoparticles for Pigmented Ultraviolet Filter Applications', *Synth. Charact. Fe Doped CeO2 Nanoparticles Pigment. Ultrav. Filter Appl.*, vol. 11, no. 5, p. 4019, 2011.

[54] R. D. Shannon, 'Revised effective ionic radii and systematic studies of interatomic distances in halides and chalcogenides', *Acta Crystallogr. Sect. A*, vol. 32, no. 5, pp. 751–767, Sep. 1976.

[55] R. C. Thomas, 'Electrogenic sodium pump in nerve and muscle cells.', *Physiol. Rev.*, vol. 52, no. 3, pp. 563–594, Jul. 1972.

[56] S Tsunekawa, S Ito, and Y Kawazoe, 'Surface structures of cerium oxide nanocrystalline particles from the size dependence of the lattice parameters', *Surf. Struct. Cerium Oxide Nanocrystalline Part. Size Depend. Lattice Parameters*, vol. 85, no. 17, pp. 3845–3847, 2004.

[57] Xuefei Wan, Daniel Goberman, Leon L Shaw, Guangshun Yi, and Gan-Moog Chow, 'Valence states of nanocrystalline Ceria under combined effects of hydrogen reduction and particle size', *Valence States Nanocrystalline Ceria Comb. Eff. Hydrog. Reduct. Part. Size*, vol. 96, no. 12, p. 123108, 2010.

[58] M Li, R Zhang, H Zhang, W Feng, and X Liu, 'Synthesis, structural and magnetic properties of CeO2 nanoparticles', *Synth. Struct. Magn. Prop. CeO2 Nanoparticles*, vol. 5, no. 2, p. 95, 2010.

[59] Laurianne Truffault *et al.*, 'Synthesis and Characterization of Fe Doped CeO2 Nanoparticles for Pigmented Ultraviolet Filter Applications', *Synth. Charact. Fe Doped CeO2 Nanoparticles Pigment. Ultrav. Filter Appl.*, vol. 11, no. 5, p. 4019, 2011.

[60] K. M. Dunnick, R. Pillai, K. L. Pisane, A. B. Stefaniak, E. M. Sabolsky, and S. S. Leonard, 'The Effect of Cerium Oxide Nanoparticle Valence State on Reactive Oxygen Species and Toxicity', *Biol. Trace Elem. Res.*, vol. 166, no. 1, pp. 96–107, Jul. 2015.

[61] 'Karakoti et al-2008-Jom-us'. .

[62] D. Cardillo, 'Haematite toxicity for 9L', 15-Aug-2016.

[63] Seung Soo Lee *et al.*, 'Antioxidant Properties of Cerium Oxide Nanocrystals as a Function of Nanocrystal Diameter and Surface Coating', *Antioxid. Prop. Cerium Oxide Nanocrystals Funct. Nanocrystal Diameter Surf. Coat.*, vol. 7, no. 11, pp. 9693–9703, 2013.

[64] C. S. Bruning-Fann and J. B. Kaneene, 'The effects of nitrate, nitrite and N-nitroso compounds on human health: a review.', *Vet. Hum. Toxicol.*, vol. 35, no. 6, pp. 521–538, Dec. 1993.

[65] G. L. Semenza, ‘HIF-1: upstream and downstream of cancer metabolism’, *Curr. Opin. Genet. Dev.*, vol. 20, no. 1, pp. 51–56, Feb. 2010.

[66] Yang Li, Wen Zhang, Junfeng Niu, and Yongsheng Chen, ‘Mechanism of Photogenerated Reactive Oxygen Species and Correlation with the Antibacterial Properties of Engineered Metal-Oxide Nanoparticles’, *Mech. Photogenerated React. Oxyg. Species Correl. Antibact. Prop. Eng. Met.-Oxide Nanoparticles*, vol. 6, no. 6, pp. 5164–5173, 2012.

[67] M. R. Folkert and R. D. Timmerman, ‘Stereotactic ablative body radiosurgery (SABR) or Stereotactic body radiation therapy (SBRT)’, *Adv. Drug Deliv. Rev.*, vol. 109, pp. 3–14, Jan. 2017.

[68] G. L. Semenza, ‘HIF-1: upstream and downstream of cancer metabolism’, *Curr. Opin. Genet. Dev.*, vol. 20, no. 1, pp. 51–56, Feb. 2010.

[69] P. E. Porporato, S. Dhup, R. K. Dadhich, T. Copetti, and P. Sonveaux, ‘Anticancer targets in the glycolytic metabolism of tumors: a comprehensive review’, *Front. Pharmacol.*, vol. 2, p. 49, 2011.